Geophys. J. Int. (0000) **000**, 000–000

Laboratory monitoring of P-waves in partially saturated sand

Julien Barrière[1], Clarisse Bordes[1], Daniel Brito[1], Pascale Sénéchal[1] and Hervé Perroud [2]

[1] *Univ Pau & Pays Adour, CNRS, TOTAL - UMR 5150*
LFC-R - Laboratoire des Fluides Complexes et leurs réservoirs
BP 1155 - PAU, F-64013, France
[2] *Univ Pau & Pays Adour, Département des Géosciences, and Laboratoire Géosciences Montpellier, UMR5243,*
CNRS-Université de Montpellier, France

22 January 2013

SUMMARY

Energy dissipation is observed on seismic data when a wave propagates through a porous medium, involving different frequency regimes depending on the nature of rock and fluid types. We focus here on the role of partial fluid saturation in unconsolidated porous media, looking in particular at P-wave phase velocity and attenuation. The study consists in running an experiment in a sand-filled tank partially saturated with water. Seismic propagation in the tank is generated in the kHz range by hitting a steel ball on a granite plate. Seismic data are recorded by buried accelerometers and injecting or extracting water controls the partial saturation. Several imbibition/drainage cycles were performed between the water and gas residual saturations. A Continuous Wavelet Transform applied on seismic records allowed us to extract the direct P-wave at each receiver. We observe an hysteresis in phase velocities and inverse quality factors between imbibition and drainage. Phase velocities and inverse quality factors are then jointly inverted to get a final poro-visco-elastic model of the partially saturated sand that satisfactorily reproduces the data. The model formulation consists in generalizing the Biot theory to effective properties of the fluid and medium (permeability and bulk modulus) in order to properly explain the phase velocity variation as a function of the saturation. The strong level of attenuation measured experimentally is further explained by an anelastic effect due to grain to grain sliding, adding to Biot's losses. This study shows that fluid distribution at microscopic scale has strong influence on the attenuation of direct P-waves at macroscopic scale and confirms that seismic prospection may be a powerful tool for the characterization of transport phenomena in porous media.

Key words: Seismic attenuation, Wave propagation, Hydrogeophysics

1 INTRODUCTION

From oilfield to near surface applications, seismic prospecting is a popular method in geophysical surveys. Nowadays, seismic imaging, besides giving structural characterizations of reservoirs, can provide informations on fluid content and distribution as in 4D monitoring (Vasco et al. 2004). Subsurface and borehole measurements (ground penetrating radar, electrical resistivity, nuclear magnetic resonance...) provide high resolution images but with a limited depth of investigation.

Seismic crosswell tomography or vertical seismic profiling enable larger volumes investigations; they are useful to perform CO_2 injection monitoring (Daley et al. 2008) or evaluate aquifer productivity (Parra et al. 2009). Sonic logging can be used as well to estimate the permeability of saturated aquifers by inverting velocity dispersion (Baron & Holliger 2011). Compressional P-wave velocities and attenuation are precisely two key parameters sensitive to fluid content and transport properties (Pride 2005), the role of fluid distribution being however not fully understood.

Interaction between fluid and solid phases during seismic propagation in porous media was originally described by Biot (1956a,b, 1962). Biot's poro-elastic theory, which describes energy dissipation due to the relative fluid/solid motion, predicts the existence of three kinds of body waves: two longitudinal (P) and one transverse (S). The faster longitudinal wave (fast P-wave) is weakly dispersive whereas the slower P-wave, the so-called "Biot's slow wave", is highly dispersive and diffusive at low frequencies. Under the common assumption that the S-wave is weakly dependent on the saturating fluid, most studies focus on the fast compressional P-wave like in the present paper.

In Biot's theory, the seismic wave propagation induces a frequency dependent relative motion of the fluid with respect to the solid matrix. The meaningful frequency f_c in that theory is the

"characteristic Biot's frequency" defined as

$$f_c = \frac{\phi\,\eta_f}{2\pi\,\gamma_0\,\rho_f\,k_0}, \tag{1}$$

where ϕ is the porosity of the medium, n_f the dynamical viscosity of the fluid, γ_0 the tortuosity, ρ_f the bulk density of the fluid and k_0 the intrinsic permeability. Table 1 gives a list and definitions of the physical parameters used throughout the paper.

Biot showed that the motion of fluid flow at $f < f_c$ is controlled by viscous shearing whereas at $f > f_c$ inertial forces dominate. He modeled the seismic attenuation or "Biot's losses" and showed that the attenuation peaks at f_c since both viscous and inertial forces are important at that particular frequency. Assumptions under the Biot theory are that the porous medium is saturated and that the wavelengths are larger than the grain size. Biot's losses are usually neglected at seismic frequencies in low permeability rocks, where f_c shifts toward ultrasonic frequencies. In unconsolidated (*i.e.* whose grains are not cemented) and highly permeable media, the relaxation frequency f_c lies in the range of [0.5 - 5] kHz and Biot's losses can be strong in the seismic to sonic frequency range, especially when pores are filled with low viscosity fluids like water.

Natural oil reservoirs or subsurface aquifers are generally not fully saturated, and interpretation of seismic data requires one to complete the Biot theory to account for partial saturation. The simplest way consists in using the original Biot's poro-elastic model and in introducing the concept of "effective fluid", a single mixture whose physical properties depend on the saturation values. This assumption is valid as long as wavelengths are larger than the size of fluid heterogeneities. In this case, the full pressure equilibration between fluids is possible during one period of wave propagation and the well-known Biot-Gassmann's relations, largely used in oil industry, are valid. When this equilibration is not totally achieved, wave induced fluid flow (WIFF) phenomena at microscopic (Mavko & Nur 1979; Dvorkin 1993; Pride et al. 2004; Gurevich et al. 2010) or mesoscopic scale (White 1975; Johnson 2001; Pride et al. 2004; Toms et al. 2006; Rubino & Holliger 2012) are considered to be the main dispersion and attenuation mechanisms. At microscopic scale, water is squeezed due to seismic wave resulting in a local flow often called "squirt flow". At a larger scale, energy is dissipated by fluid pressure diffusion between mesoscopic patches of gas (greater than the grain size but smaller than the wavelength) and the surrounding water. In consolidated and/or poorly permeable rocks, squirt flows can be strong at ultrasonic frequency (Gurevich et al. 2010), but some mesoscopic flows taking place in unconsolidated and/or highly permeable rocks can also induce such a mechanism at seismic frequencies.

Since grains are not cemented in sands and soils, energy dissipation mechanisms at the grain to grain contact (Stoll & Bryan 1970; Duffaut et al. 2010) are also considered since frictional dissipation can occur in porous media (Walsh 1966; Johnston et al. 1979). These phenomena, due to the grain contact stiffness, depend on the confining pressure and may lead to a strong attenuation. A physical formulation is obtained in light of well-known models proposed by Mindlin (1949) or Walton (1987) where the medium is idealized as a random packing of identical spheres. At confining pressure lower than 5 MPa (Duffaut et al. 2010), contacts are smooth allowing slipping between grains with friction losses, even for small strains involved in seismic wave propagation. The grain to grain attenuation mechanism is considered as independent of the frequency and leads to a strong increase of the inverse quality factor Q^{-1} (defined as the loss of energy occurring during one wave period). Stoll & Bryan (1970) added friction losses in the Biot theory with a non-dispersive phase velocity, implying non causal frame behavior (Turgut 1991). Keller (1989) overcame this difficulty by applying a visco-elastic constant-Q model (Kjartansson 1979) and obtained a good agreement with experimental data in saturated sand. Recent models (Chotiros & Isakson 2004; Kimura 2006) suggest that the grain to grain contact should include microscopic fluid flow in unconsolidated sediments. Hefner & Williams (2006) confirmed that the total frame losses can be estimated by the simplest constant-Q model within a general framework of Biot's theory.

Laboratory experiments provide data in controlled media and are thought to be an opportunity to provide a better understanding of attenuation and dispersion of P-waves in porous media. Investigating experimentally the role of fluid content, viscosity, size of heterogeneities and/or permeability are current challenges (Muller et al. 2010). Resonant bar and stress/strain phase difference, which were inherited from historical studies in rock mechanics, provided some reference studies on saturation effects at low frequency (below 10 kHz). Among them, Winkler & Plona (1982) and Murphy (1982) showed by the resonant bar method that partial saturation induces a strong attenuation in the kHz range. Later, Cadoret et al. (1998) showed that this could be attributed to mesoscopic gas patches appearing during drainage. Using stress/strain methods at frequencies lower than 1 kHz, Batzle et al. (2006) highlighted the importance of fluid mobility (ratio of intrinsic permeability to fluid viscosity) on dispersion and attenuation. All these experiments are performed in rocks and do not enable to observe the wave propagation. The generalization of these results into seismic field measurements remains challenging and scaling effects are still under debate.

Another experimental approach consists in using ultrasonic transducers in the [0.05 - 5] MHz range (Bourbié et al. 1987), especially in order to focus on the WIFF and fluid heterogeneities in consolidated rocks (Gregory 1976; Gist 1994; Murphy 1984; Mavko & Nolen-Hoeksema 1994; Walsh 1995; King et al. 2000). Recent studies showed that mesoscopic patches are created during drainage process implying strong differences of velocity (Cadoret et al. 1995; Monsen & Johnstad 2005; Lebedev et al. 2009) contrary to imbibition where the saturation is more homogeneous. Other studies (Domenico 1977; Berge & Bonner 2002) in unconsolidated media showed that the effective fluid model remains valid in this high frequency range even if some discrepancies can be attributed to microscopic patchy saturation at high pressure and water saturation. At lower frequencies (20 kHz), George et al. (2009) showed that the seismic velocity and attenuation strongly depend on the fluid saturation history in compacted heterogeneous soils similarly to some observation in rocks (Cadoret et al. 1995, 1998). For unconsolidated media, many laboratory datasets exist but they were mainly obtained on dry, saturated or nearly-saturated sediments (Prasad 1992; Bardet & Sayed 1993; Ayres & Theilen 2001; Prasad 2002).

In the following, we perform an experimental study specifically designated to analyse and understand the wave propagation and its attenuation through a partially saturated non-consolidated porous media. We want to unravel seismic attenuation mechanisms in such partially saturated media and look in particular at the validity of the Biot theory extended to a partially saturated media. In this paper, we describe a laboratory experiment involving the propagation of direct P-waves in the kHz range in a sand-filled tank partially saturated. The quite slow P-wave velocity (around 160 m/s) in sand allows us to perform far field measurements in a 1-m long sample since wavelengths are around 0.1 m for a working fre-

Notation	Physical parameter	Units	Expression or ref.
	Biot's theory and effective fluid model		
γ_0	Tortuosity	dimensionless	
η_f	Dynamic viscosity of the (effective) fluid	Pa.s	
Λ	Pore shape	dimensionless	$\Lambda^2 = \frac{\xi \gamma_0 k_0}{\phi}$
ϕ	Connected porosity	dimensionless	
μ	Frame shear modulus	Pa	
ρ	Total bulk density of the medium	kg.m^{-3}	
ρ_f	Density of the fluid	kg.m^{-3}	
ρ_g	Density of gas (air at atmospheric pressure)	kg.m^{-3}	
ρ_s	Density of solid (grains)	kg.m^{-3}	
ρ_w	Density of water	kg.m^{-3}	
ξ	Geometry parameter	dimensionless	$\xi = 8$ from Pride (2005)
ω_c	Biot's characteristic pulsation	rad.s^{-1}	$\omega_c = 2\pi f_c$
C	Coupling modulus	Pa	equation (9)
F	Viscodynamic factor	dimensionless	
f_c	Biot's characteristic frequency	Hz	(1)
H	P-wave undrained modulus	Pa	(11)
K_f	Bulk modulus of the fluid or mixture	Pa	sections 2.1 and 2.2
K_w	Bulk modulus of water	Pa	
K_g	Bulk modulus of gas	Pa	
K_U	Undrained bulk modulus	Pa	
k_0	Intrinsic permeability	m^2	
M	Fluid-storage coefficient	Pa	(9)
m	Virtual mass	kg.m^{-3}	$\gamma_0 \rho_f / \phi$ and (2)
m'	Viscodynamic operator	kg.m^{-3}	(7)
S_w	Water saturation	dimensionless	
	Walton's model		
μ_S	Shear modulus of the solid (grains)	Pa	
K_S	Bulk modulus of the solid (grains)	Pa	
C_s	Compliance parameter	Pa^{-1}	(18)
K_D	Drained bulk modulus	Pa	(17)
n_0	Number of grain to grain contacts at P_0		
P_0	Critical effective pressure	Pa	
P_c	Confining pressure	Pa	
P_e	Effective pressure	Pa	
P_f	Pore fluid pressure	Pa	
	Visco-elastic model		
μ^*	Complex frequency-dependant shear bulk modulus		(19)
$\omega_0/2\pi$	Reference frequency		(19)
K_D^*	Complex frequency-dependant frame bulk modulus		(19)
Q_μ	Shear losses quality factor		(19)
Q_{K_D}	Bulk losses quality factor		(19)
	Effective permeability		
k_e	Effective permeability	m^2	(26)
kr_w	Relative water permeability	dimensionless	(26)
kr_g	Relative gas permeability	dimensionless	(26)
S_{g0}	Gas residual saturation	dimensionless	
S_{w0}	Water residual saturation	dimensionless	

Table 1. List of the physical parameters used throughout the paper.

quency near 1.6 kHz, these wavelengths being one thousand times larger than the grain size. Similar experimental set-up were used to characterize fresh mortar (Sénéchal et al. 2010) and record seismo-electric and seismomagnetic phenomena (Bordes et al. 2006, 2008). The purpose of our experiment is to extract direct P-waves from seismic signals in order to monitor seismic dispersion and attenuation during two distinct saturation modes: imbibition and drainage. We give a theoretical background in part 2 on seismic wave propagation in unconsolidated and partially saturated media based on the general framework of Biot's theory. The experimental set-up, the measurement and data processing techniques are described in part 3. The experimental results are discussed and analyzed under the frame of a combined poro-visco-elastic model in part 4.

2 THEORETICAL BACKGROUND

Among many theoretical developments on wave propagation in porous media, the Biot theory (Biot 1956a,b, 1962) is often considered as the most appropriate for unconsolidated media. That theory was extensively used and improved by marine geophysicists (Stoll & Bryan 1970; Stoll 1977; Buchanan 2006; Hefner & Williams 2006). In the following, we give the general formulation of this model for a fully saturated medium. Then, some mixing laws are presented to take into account the mixture of two saturating fluids for varying effective pressure. The grain to grain losses are eventually introduced by considering a visco-elastic component in poro-elastic moduli.

2.1 Losses from relative motion between fluid and solid phases

For a saturated porous medium, dilatational wave propagation can be described by two governing wave equations which take into account the fluid/solid couplings generated by seismic displacements. These equations of motion for an isotropic and homogeneous poro-elastic medium can be expressed for longitudinal P-waves as (Biot 1962; Stoll 1977):

$$\begin{cases} H\nabla^2 e - C\nabla^2\zeta = \dfrac{\partial^2}{\partial t^2}(\rho\, e - \rho_f\, \zeta) \\ C\nabla^2 e - M\nabla^2\zeta = \dfrac{\partial^2}{\delta t^2}(-\rho_f\, e + m\, \zeta) - F\, \dfrac{\eta_f}{k_0}\, \dfrac{\partial \zeta}{\partial t}, \end{cases} \tag{2}$$

where H, M, C are poro-elastic moduli described below, η_f is the dynamic viscosity of the fluid, k_0 the intrinsic permeability, ρ the total bulk density defined in the saturated medium by $\rho = (1-\phi)\rho_s + \phi\rho_f$ with ρ_f the fluid density and ρ_s the solid grain density, the virtual mass m being defined in Table 1. The volume dilatation e and the accumulation or depletion of fluid ζ (often called "increment of fluid content") are respectively e=$\nabla.\mathbf{u}$ where $\mathbf{u}$ is the solid phase displacement and ζ=$-\nabla.\mathbf{w}$ where $\mathbf{w}$ is the relative motion of the fluid with respect to the frame. This relative displacement is defined by $\mathbf{w}$=$\phi(\mathbf{u}-\mathbf{U})$ where $\mathbf{U}$ is the fluid phase displacement.

In the case of plane dilatational P-waves propagating in the x-direction, e and ζ have the following form

$$\begin{cases} e = \nabla.\mathbf{u} = A_e\, e^{i\omega\,(t - s_P\, x)} \\ \zeta = -\nabla.\mathbf{w} = A_\zeta\, e^{i\omega\,(t - s_P\, x)}, \end{cases} \tag{3}$$

where ω is the angular frequency and s_P is the P-wave slowness. A_e and A_ζ are respectively the amplitudes of the volume dilation and increment of fluid content. A condition for the existence of a solution to equation (2) is that the determinant

$$\begin{vmatrix} Hs_P^2 - \rho & \rho_f - Cs_P^2 \\ Cs_P^2 - \rho_f & m - Ms_P^2 - i\dfrac{\eta_f}{k_0}\dfrac{F}{\omega} \end{vmatrix} \tag{4}$$

vanishes in order to obtain non-zero values for A_e and A_ζ. That leads to a quadratic equation whose roots for s_P correspond to the fast and slow P-waves complex slownesses. Considering only the fast one, the complex slowness s_P is expressed in the following form :

$$s_P = \sqrt{\frac{\rho M + m'H - 2\rho_f C - \sqrt{A}}{2(HM - C^2)}}, \tag{5}$$

where

$$A = (m'H - \rho M)^2 + 4(\rho_f H - \rho C)(\rho_f M - m'C), \tag{6}$$

and

$$m' = \frac{\gamma_0}{\phi}\rho_f - i\frac{\eta_f}{k_0}\frac{F}{\omega}, \tag{7}$$

γ_0 being defined as the tortuosity of the porous medium.

In Biot's theory, the mechanical coupling or friction between fluid and solid has a frequency dependence characterized by the viscodynamic factor F (Carcione 2001). Johnson et al. (1987) proposed a formulation of F related to the pore shape parameter Λ^2 (see Table 1)

$$F = \sqrt{1 + \frac{4i\gamma_0^2 k_0}{\chi \Lambda^2 \phi}} \qquad \text{where} \qquad \chi = \frac{\eta_f \phi}{k_0 \rho_f \omega}, \tag{8}$$

a formulation valid when wavelengths are larger that the pore size.

Following expressions (8), variations in the fluid's properties or variations in the permeability induce changes in frictions forces and, in turn, changes in the viscodynamic factor F. These variations can occur, for example, during imbibition or drainage processes due to water content changes (see part 2.2 and part 4.3 for the analytical formulation).

The poro-elastic moduli H, M, C, can be expressed in a more comprehensive way (Pride 2005) as function of the well-known K_U, K_D and B moduli. The "undrained bulk modulus" K_U is the porous media uncompressibility measured by applying a stress on a sealed sample. The "drained bulk modulus" K_D is measured by applying a stress on an open sample, which implies that the fluid pressure does not change. The "Skempton's coefficient" or modulus B (Skempton 1954), corresponds to the ratio of the undrained fluid pressure over the confining pressure. The moduli C and M are defined by

$$C = BK_U \qquad \text{and} \qquad M = \frac{BK_U}{\alpha}, \tag{9}$$

where α is the "Biot-Willis constant" (Biot & Willis 1957) defined by

$$\alpha = \frac{1 - K_D/K_U}{B}. \tag{10}$$

The modulus M is called the "fluid-storage coefficient" and C the "coupling modulus" (Biot 1962). H, sometimes called the "P-wave undrained modulus", is defined by

$$H = K_U + \frac{4}{3}\mu \tag{11}$$

assuming that the fluid has no influence on the frame shear modulus μ.

When solid grains are made of homogeneous and isotropic elastic media, the Gassmann's relations (1951) stipulate that the coefficients B and K_U are real and frequency-independent. They depend therefore only on the drained modulus K_D, on the bulk modulus of the grains K_S and on the bulk modulus of the fluid K_f:

$$\begin{aligned} B &= \frac{1/K_D - 1/K_S}{1/K_D - 1/K_S + \phi(1/K_f - 1/K_S)}, \\ K_U &= \frac{K_D}{1 - B(1 - K_D/K_S)}. \end{aligned} \tag{12}$$

Finally, the phase velocity V_P and the inverse quality factor Q_P^{-1} are deduced by their usual expressions

$$\begin{cases} V_P(\omega) = 1/\Re[s_P], \\ Q_P^{-1}(\omega) = 2\dfrac{\Im[s_P]}{\Re[s_P]} = \dfrac{2a_P(\omega)V_P(\omega)}{\omega}, \end{cases} \tag{13}$$

where $\Re(\,)$ and $\Im(\,)$ are respectively the real and imaginary parts of complex numbers and a_P is the attenuation coefficient.

As a conclusion, using the Gassman's relation (12) described above, we need to know on the one hand the poro-elastic moduli K_D, K_f, K_S and μ , and on the other hand the physical properties ρ, ρ_f, η_f, k_0 in order to determine $V_P(\omega)$ and $Q_P^{-1}(\omega)$ from (13) .

2.2 Effective fluid model ρ_f, η_f, K_f

In the previous section, the subscript $_f$ was referring to a monophasic fluid since the medium was saturated under Biot's theory. From now on, $_f$ accounts instead for the mixture of two fluid phases since we are interested by partial saturation in the present paper. We use the water saturation values S_w which characterizes the ratio of pores filled by water. The density ρ_f of the mixture becomes a linear average of each fluid density

$$\rho_f = \rho_g(1 - S_w) + \rho_w S_w. \tag{14}$$

Considering that a linear average of gas and water viscosities (η_g and η_w respectively) overestimate the effective viscosity (η_f), we use instead

$$\eta_f = \eta_g \left(\frac{\eta_w}{\eta_g}\right)^{S_w} \tag{15}$$

as proposed by Teja & Rice (1981).

An effective fluid bulk modulus can also be computed using

the Wood's harmonic average of gas K_g and water K_w bulk moduli (Wood 1955)

$$\frac{1}{K_f} = \frac{1-S_w}{K_g} + \frac{S_w}{K_w}. \tag{16}$$

This last relation only applies if a pressure equilibration between the two fluids happens during the wave propagation. Indeed, this so-called "uniform saturation" is only valid when the fluid phases are mixed at a sufficiently fine scale compared to the wavelength (Berryman et al. 1988).

The properties of the monophasic fluid in equations (1) to (12) can now be substituted for the effective fluid model parameters in equations (14), (15) and (16) in order to account for partial saturation.

2.3 The frame moduli K_D and μ

The frame moduli K_D and μ are intrinsic properties of the medium that depend on the effective pressure $P_e = P_c - P_f$ where P_c and P_f are respectively the confining pressure and the pore fluid pressure. K_D gets larger when an increasing confining pressure leads to new grain to grain contacts (compaction effect); conversely, K_D decreases when the pore fluid pressure increases (swelling effect). In unconsolidated porous media, the frame modulus can be estimated by using the Walton's theory (1987) or by its modified version given by Pride (2005):

$$K_D = \frac{1}{6}\left[\frac{4(1-\phi)^2 n_0^2 P_0}{\pi^4 C_s^2}\right]^{1/3}\left[1+\left(\frac{16P_e}{9P_0}\right)^4\right]^{-1/24}\frac{P_e}{P_0}^{1/2}. \tag{17}$$

In random sand packs, $P_0 = 18$ MPa is a critical effective pressure beyond which, even if P_e increases, the number of contacts per grain remains around $n_0 = 9$. C_s is the compliance parameter and is linked to the bulk modulus K_S and the shear modulus μ_S of solid grains:

$$C_S = \frac{1}{4\pi}\left(\frac{1}{\mu_S} + \frac{1}{K_S + \mu_S/3}\right). \tag{18}$$

Pride (2005) recommends to deduce the frame shear modulus from the relation $\mu = 3K_D/5$, a reasonable assumption in unconsolidated porous media.

2.4 V_P and Q_P^{-1} predictions from Biot's theory extended to partial saturation

Using Biot's original theory developed in section 2.1, the effective fluid properties developed in section 2.2 and the Walton's theory to estimate K_D and μ (see section 2.3), we computed the predicted phase velocities V_P and inverse quality factor Q_P^{-1} as a function of frequency and water saturation (Figure 1). The parameters used in the computation are given in Table 2 and correspond to the physical properties of the partially saturated sand used in our experiment. The computation is performed for $f = [10-10^4]$ Hz, $S_w = [0-1]$ and for a negligible pore pressure, *i.e.* $P_f = 0$. Biot's frequency f_c defined in equation (1) is also represented in Figure 1: f_c significantly varies with the water saturation since it depends on the effective fluid density and viscosity.

Figure 1a) shows a global decrease (around 4 %) of the phase velocity in the range $S_w \simeq [0-0.85]$ mainly due to the increase of the total bulk density with the water saturation as observed by Bachrach & Nur (1998). For higher water saturation, the phase velocity increases abruptly due to a strong increase of K_f since air bubbles do not contribute anymore to the compressibility of the fluid. For frequencies above 500 Hz, Figure 1b) shows a local maximum in Q_P^{-1} around $S_w = 0.8$. It is clear in Figure 1b) that the maximum attenuation of P-waves closely follows Biot's critical frequency, as expected. Note that when the medium is fully saturated at $S_w = 1$, Q_P^{-1} is also very high.

The phase velocities of direct P-waves in Figure 1a) are around 160 m/s near our experimental working frequency 1.6 kHz. That frequency, being relatively close to f_c in the S_w range explored experimentally (see section 3.1), is therefore well suited to observe attenuation phenomena due to Biot's losses.

2.5 The role of friction losses at the grain to grain contact

As long as a frame is considered to be an elastic medium, poroelastic moduli H, M, C are real and frequency independent. However, wave propagation through an unconsolidated porous medium can involve anelastic effects due to grain to grain sliding (Biot 1962; Stoll & Bryan 1970). These frame losses imply that the moduli K_D and μ (and consequently H, M, C and B, see section 2.1) become complex and frequency dependent. These effects may be modeled by a linear visco-elastic behavior of the medium characterized by a constant-Q (Kjartansson 1979). This new visco-elastic component of attenuation adds to Biot's losses described in section 2.1. The final expressions of the complex and frequency-dependent frame bulk and shear moduli K_D^* and μ^*, satisfying causality constraints of Kramers-Kronig relations, are:

$$\begin{aligned} K_D^* &= K_D\left(i\frac{\omega}{\omega_0}\right)^{2\gamma_{K_D}} \quad \text{where} \quad \gamma_{K_D} = \frac{\arctan(Q_{K_D}^{-1})}{\pi}, \\ \mu^* &= \mu\left(i\frac{\omega}{\omega_0}\right)^{2\gamma_\mu} \quad \text{where} \quad \gamma_\mu = \frac{\arctan(Q_\mu^{-1})}{\pi}, \end{aligned} \tag{19}$$

where Q_{K_D} and Q_μ are respectively the quality factor for shear losses and bulk losses, and $\omega_0/2\pi$ is the reference frequency of the constant-Q model. This formulation is valid in a narrow range around the reference frequency since the corresponding P-wave velocities vary linearly in frequency with a slope $(2\pi/\omega_0)$. As already mentioned in section 2.3, the smooth limit of Walton's model, which enables slipping contacts, implies $\mu = 3K_D/5$ and corresponds to a Poisson's ratio around 0.25 for the equivalent isotropic and elastic frame. The quality factors Q_μ and Q_{K_D} are here linked by the same relation $Q_\mu = 3Q_{K_D}/5$. This simplified visco-elastic model is generally used to explain strong levels of attenuation observed in non-compacted sands which cannot be interpreted as pure Biot's losses (Keller 1989; Hefner & Williams 2006). In practice, using this model consists in setting a value of ω_0 close to the working frequency and then infer an absolute value of Q_{K_D} from the attenuation data, as we will see in section 4.4.

3 EXPERIMENTAL APPARATUS

Taking into account alll the theoretical considerations seen in part 2, we have designed an experiment in order to study the monitoring of direct P-waves propagating in a highly permeable and non-compacted sand. The main objective was to compare phase velocities and inverse quality factors deduced from experimental data to the Biot theory extended to a partially saturated medium.

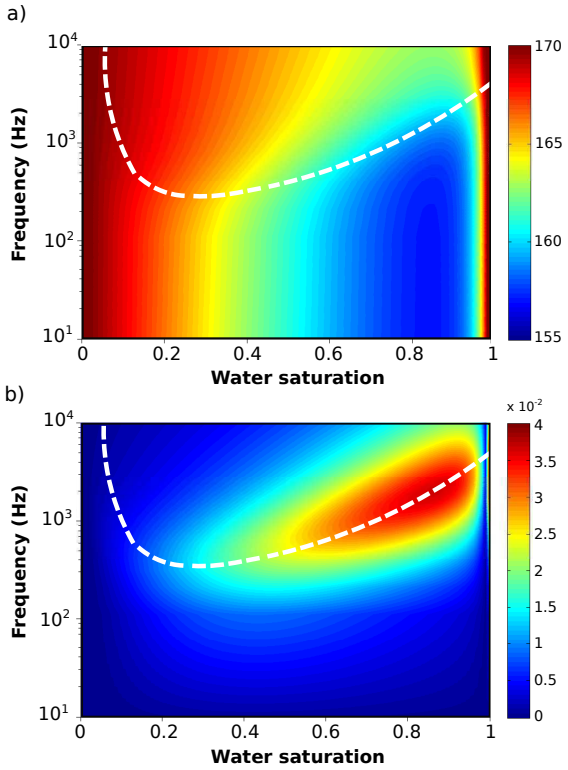

Figure 1. a) Phase velocities V_P in m/s and b) inverse quality factors Q_P^{-1} as a function of the frequency and the water saturation. The computations are performed using Biot's theory extended to an effective fluid and Walton's model to estimate K_D. The physical parameters of this calculation are given in Table 2. Biot's frequency in dashed white line in both figures varies with the water saturation since it depends strongly on the effective fluid density and viscosity.

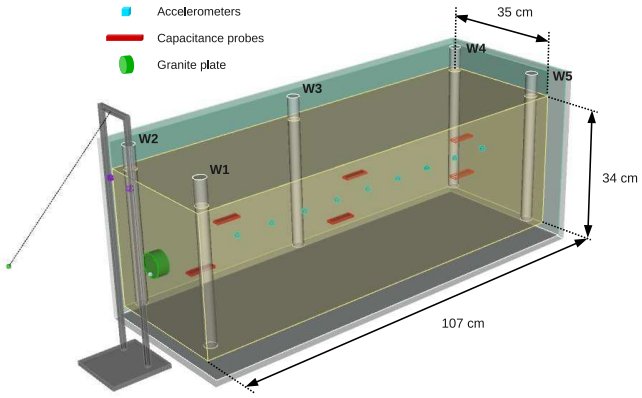

Figure 2. Schematic view of the experimental set-up. A steel ball mounted on a pendulum hits a circular granite plate on the left lateral side of the sand-filled tank. Wave propagation is monitored by nine aligned buried accelerometers. Water saturation level is measured by capacitance probes. Five wells W1-W5 are used to proceed to imbibition or drainage.

3.1 Experimental set-up

The experimental set-up, sketched in Figure 2, is a wood rectangular container whose inner volume is $(1.07 \times 0.4 \times 0.35)$ m^3. It is filled with a volume of sand (34-cm height) introduced at a constant flow using a large sieve. Lateral sides of the container are covered by a 3-cm thickness acoustic foam in order to attenuate boundary reflections. The sand is pure silica ($\geq$ 98%) with homogeneous grain size distribution of mean diameter d_m = 249 μm extracted from a sandpit in the South-West of France (Landes).

The bulk density of the solid grains ρ_S varies between 2635 and 2660 kg.m^{-3}. The porosity, measured by weighting 4 dried samples, is 0.4 $\pm$ 0.02 for ρ_S = 2650 kg.m^{-3}. The corresponding bulk density of the dry sand ρ is therefore 1588 $\pm$ 53 kg.m^{-3}. Other physical parameters of the sand are given in Table 2, some of them being measured, some others being theoretically inferred or provided by the sandpit factory data.

On one side of the container in Figure 2, a granite disk at 17-cm depth from the free surface is both coupled mechanically to the sand and isolated from the container in order to avoid wave propagation through the container boundaries. The steel ball of a pendulum hits the granite plate and generates seismic propagation throughout the sand. Nine IEPE piezoelectric accelerometers (500 mV/g in the [10^{-3} -10^4] Hz range) are buried in the sand, aligned with the granite disk in the horizontal axis of the source. These accelerometers are 10-cm spaced with offsets (source-receiver distances) varying from 20 to 100 cm. The saturation measurements are performed by six calibrated capacitance probes also located at 17-cm depth. Data acquisition is performed by a 24 bits/16 channels recorder at a 200 kHz sampling rate.

Three imbibition/drainage cycles are performed by injecting or sucking water into 5 wells (W1 to W5 in Figure 2). We make sure to use water at equilibrium with sand by flowing deionized water into the sand until the conductivity of the fluid reaches a stable value around 117 μS.cm^{-1} before starting the experiment. Injection pressure is obtained by uplifting water containers at 40-cm height above the tank. Imbibition is performed by injecting water through the wells W2, W3 and W5 whereas drainage is performed by extracting water through the wells W1, W3 and W4.

An initial complete cycle is performed to homogenize pore

Medium	Parameters	Notations	Values with units	Reference
Grain	diameter	d_m	2.49×10^{-4} m	*
	density	ρ_S	2.65×10^{3} kg·m^{-3}	*
	bulk modulus	K_S	3.6×10^{10} Pa	*
	shear modulus	μ_S	4.4×10^{10} Pa	*
Water	density	ρ_w	9.98×10^{2} kg·m^{-3}	
	bulk modulus	K_w	2.5×10^{9} Pa	
	viscosity	η_w	10^{-3} Pa.s	
Gas (air)	density	ρ_g	1.2 kg·m^{-3}	
	bulk modulus	K_g	$1.5.10^{5}$ Pa	
	viscosity	η_g	1.10^{-5} Pa·s	
Frame	porosity	ϕ	0.4	measured
	permeability	k_0	1.02×10^{-11} m^2	measured
	tortuosity	γ_0	1.75	Berryman (1981)
	bulk modulus	$K_D(P_f = 0)$	2.5×10^{7} Pa	Walton (1987); Pride (2005)
	shear modulus	μ	1.54×10^{7} Pa	$\mu = 3K_D/5$

* *From sandpit data sheet*

Table 2. Parameters involved in Biot's theory.

fluid distribution: a first imbibition starts from oven-dried sand and is followed by a first drainage. In the next two cycles, the imbibition and drainage last for more than an hour and span water saturation range from $S_{w0} = 0.3$, the water residual saturation, to $S_w = 1 - S_{g0} = 0.9$, the water saturation at the gas residual saturation. We assume that the water flow during cycles is slow enough to consider that seismic monitoring is done in a quasi-static state. For each cycle, we perform a time-lapse monitoring by repeating 25 times: an initial saturation measurement followed by ten seismic records and a final saturation measurement.

3.2 Typical seismic record and numerical validation of the experimental set-up

An example of raw data presented in Figure 3 shows that recorded waveforms during an experiment of drainage are quite complex and that many different waves seem to be recorded. In order to make sure that direct P-waves are not mixed with others reflected waves from the free surface, we used the 2D Specfem2D numerical code based on the spectral element method (Komatitsch & Vilotte 1998; Tromp et al. 2008) to simulate the experiment. The partially saturated sand is defined as an equivalent visco-elastic medium where P and S-waves propagate respectively at 150 m.s^{-1} and 86.5 m.s^{-1}, corresponding to a Poisson's ratio of 0.25 and a bulk density equal to 1800 kg.m^{-3}. Zener model (also called Standard Linear Solid model) is used for the description of the visco-elastic behaviour, with bulk and shear quality factors $Q_K \simeq 20$ and $Q_S = 3Q_K/5 \simeq 12$ respectively, *i.e.* a strongly attenuating medium. The result of the Specfem2D computation shown in Figure 4 was performed by assuming a free surface at the top of the container in one case (solid line case), and by assuming a strongly attenuating upper boundary in a second case (dashed line case). We conclude from these synthetic seismograms that the direct P-waves should be clearly identified experimentally since the first arrival is very well distinguished from latter arrivals. The raw data presented in Figure 3b) (the first milliseconds of the seismogram) confirms qualitatively this last point with a very clear first arrival on the first accelerometers, followed two milliseconds later by another clear wave which could be a reflection. It indicates that the acoustic foam does not act as a perfectly absorbing material. Even if numerical simulations cannot reproduce quantitatively the experimental seismograms, the qualitative comparison confirms that direct P-waves are not mixed with reflected waves when the measurements are performed at mid-depth of the tank.

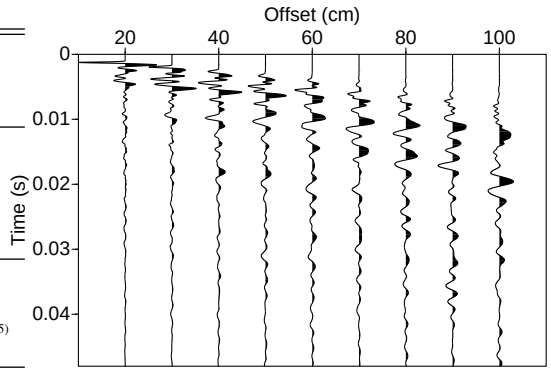

a)

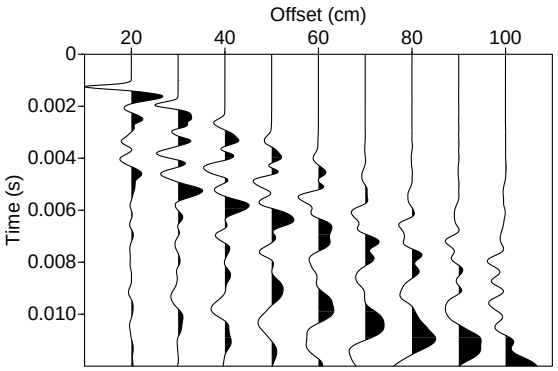

b)

Figure 3. a) An example of observed seismogram recorded by the nine accelerometers in the sand-filled tank during the beginning of the third drainage, for $S_w \simeq 0.88$. The signals are trace by trace normalized. b) Zoom on the first 10 milliseconds of the seismogram shown in a).

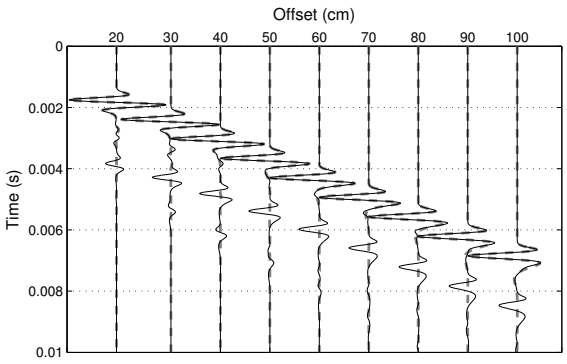

Figure 4. Numerical simulation performed with Specfem2D of propagative waves in the experimental device. The dashed line is the result of a calculation performed with an attenuating boundary at the top of the container whereas the solid black line is performed with a free surface. Reflections on the free surface have important amplitudes but are not mixed with the first arrivals. For better visualization, each seismic trace is normalized by the maximum amplitude of the "rigid upper boundary" case.

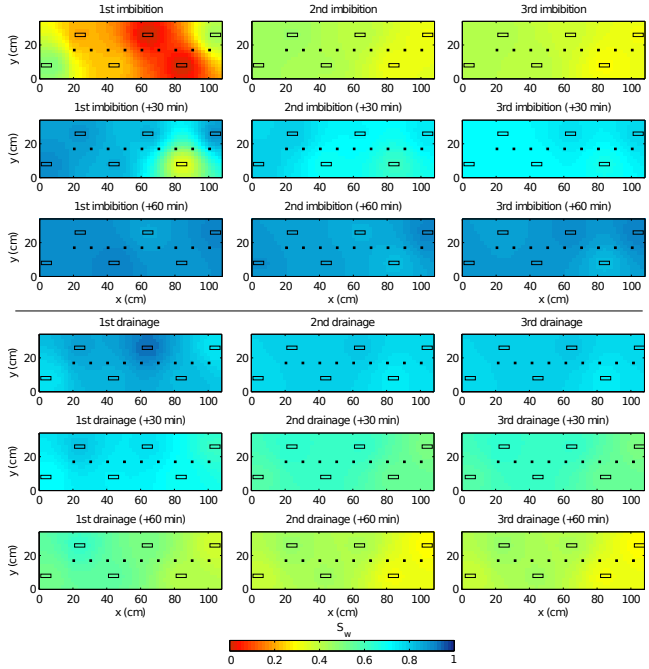

Figure 5. Water saturation S_w intensity maps obtained during the three cycles of imbibition/drainage. For each imbibition/drainage, three maps are shown: the first one at time $t = 0$, the second at time $t = 30$ minutes and the last one at time $t = 60$ minutes. The maps are computed at 17-cm depth (from the top) in the horizontal plane containing the nine accelerometers (dots) and the six capacitance probes (rectangles). They are obtained by interpolating spatially the capacitance probes measurements using the IDW method.

3.3 Saturation monitoring

In order to relate attenuation and dispersion phenomena to water saturation S_w, it was necessary to reconstitute spatial saturation maps in the horizontal plane containing the six capacitance probes during all the imbibition/drainage cycles. For this purpose, that plane is divided into a grid of 17 lines (x-direction) and 55 rows (y-direction). Using the Inverse Distance Weightering method (IDW) developed by Shepard (1968), we obtain the saturation maps by interpolating S_w at each node using

$$S_w(x,y) = \frac{\sum_{j=1}^{N} \frac{S_{wj}(x,y)}{h_j^2}}{\sum_{j=1}^{N} \frac{1}{h_j^2}}, \qquad (20)$$

where $h_j = \sqrt{(x-x_j)^2 + (y-y_j)^2}$ and $N = 18$ is the number of nodes where the saturation is known since they contain the capacitance probes (each probe occupies three nodes).

The eighteen saturation maps obtained during the three imbibition/drainage cycles are shown in Figure 5. As previously mentioned, the first imbibition consists in injecting the equilibrated water into the oven-dried sand and results in a strongly heterogeneous fluid distribution. The first drainage bring the sand at the water residual saturation S_{w0}; seismic monitoring measurements can then begin. During the two following cycles, the water saturation variations for each map are below the probe uncertainty (from ± 0.025 at $S_w = 0.9$ to ± 0.05 at $S_w = 0.3$); the water saturation can therefore be considered as always spatially homogeneous in the horizontal plane of measurements during cycles 2 and 3.

3.4 Extraction of phase velocities and quality factors

Estimations of body-waves velocity dispersion are usually performed in laboratories at ultrasonic frequencies by using the cross-spectrum method (Wuenschel 1965; Winkler & Plona 1982; Molyneux & Schmitt 2000). This method requires to capture the waveform at two different source-receiver distances along the same ray path. It can be applied in the Fourier domain as well as in the continuous wavelet transform (CWT) domain. The CWT is a windowing technique which enables a time-frequency representation of non-stationary signals (Lang & Forinash 1998; Reine et al. 2009; Kazemeini et al. 2009). In the present study, the phase velocities are measured by picking, in the time-frequency domain obtained by CWT, the phase differences between two accelerometers. A standard Morlet wavelet is chosen in order to ensure a linear transformation that is necessary for phase velocity analysis (Barrière 2011).

The extraction of attenuation coefficients is obtained as well by comparing amplitude spectra on several accelerometers. In an homogeneous medium, the amplitude A of a spherically divergent P-wave at distance r from the source is given by

$$A(f) = \frac{A_0(f) r_0}{r} e^{-a(f)(r-r_0)}. \qquad (21)$$

A_0 and r_0 in (21) are respectively the amplitude and the distance from the source at a reference offset, $a(f)$ is the frequency dependent attenuation coefficient defined as $a = (\pi f)/(V_P Q_P)$ where V_P is the P-wave phase velocity and Q_P the P-wave quality factor, consistently with the general expression of V_P and Q_P given in equation (13). Equation (21) remains valid if $Q_P > 1$ (Futterman 1962). By considering the two amplitudes A_1 and A_x of the first lobe, respectively at the first accelerometer and any other, the ratio of these amplitudes is given by

$$\log \frac{A_1(f)}{A_x(f)} - \log \frac{r_x}{r_1} = \frac{\pi f}{V_P(f) Q_P(f)} d_x, \qquad (22)$$

where r_1 and r_x are the source-accelerometer distances. Expression (22) enables us to determine the quality factor Q_P by computing the slope $\pi f/[V_P(f)Q_P(f)]$ of the linear relation as a function of $d_x = (r_x - r_1)$. The ratio r_x/r_1 corresponds to the geometrical spreading term valid in the far field domain where amplitude decreases approximatively as a function of $1/r$.

The equation (22), known as the "spectral ratio", is usually written as a simple linear function of f, which implies that Q_P and V_P are independent of the frequency in the linear part of the spectral ratio. However, a frequency dependent P-wave quality factor is predicted by the Biot theory and observed in the seismic to sonic frequencies range in sandy sediments (Badiey et al. 1998). As proposed by Jeng et al. (1999), the spectral ratio can then be calculated using equation (22) in order to take into account the frequency dependence. We apply therefore equation (22) to compute Q_P from the records of the aligned buried accelerometers in the experiment.

3.5 Experimental constraints

In our experiment we want to measure and analyze the behavior of the direct P-waves; however, pure longitudinal displacements can only be precisely recorded in the far field. Indeed, in the near field, compressive and shear motions are combined and can hardly be distinguished (Aki & Richards 2002). Recent studies have demonstrated that analyzing seismic data in the near field can lead to a biased P-wave quality factor in shallow seismic investigations due to a strong geometrical spreading (Haase & Stewart 2010; Mangriotis et al. 2011).

In order to keep a consistent analysis of phase velocity and quality factors, it is then necessary to make sure that the receivers are in the far field. For a spherically divergent P-wave, far-field conditions apply for $r \gg \lambda_P/2\pi$ where λ_P is the wavelength and r the source-receiver distance (Haase & Stewart 2010). We chose to adopt the criterion $r > 2\lambda_P$ which is satisfied in our experiment for frequencies larger than 1.6 kHz (considering the highest measured velocity around 160 m/s). That gives the lower limit of the experimental working frequencies.

The upper working frequency limit is based upon a magnitude criterion on the amplitude spectrum : $A(f) \geq A_{max}/2$ where A_{max} is the maximum magnitude of the amplitude spectrum obtained at the most distant accelerometer. This condition is fully satisfied for frequencies lower than 1.8 kHz to 2 kHz depending on the saturation values. The frequency band used for attenuation and velocity data processing is therefore chosen as [1.6 - 1.8] kHz. In this narrow frequency band, phase velocity and quality factor variations are *a priori* only due to variations of intrinsic properties such as the variation of water content.

As said previously, the present study consists in a seismic monitoring using direct P-waves which have to be isolated from other arrivals. A complete study has been performed in the CWT domain and showed that the detection of the direct P-wave becomes uncertain from the seventh accelerometer (Barrière 2011). The linear regression to estimate the quality factor using equation (22) is consequently performed from the first to the sixth accelerometer, these regressions giving a high correlation coefficient R^2 up to 0.9. For the P-wave phase velocity computation the first two accelerometers were used.

4 EXPERIMENTAL RESULTS AND DISCUSSION

The measured phase velocities V_P and inverse quality factors Q_P^{-1} retrieved using the data processing described in section 3.4 are summarized in Figure 6. Those measurements performed sequentially during the second imbibition and drainage (I2 and D2 respectively) and during the third imbibition and drainage (I3 and D3 respectively), are presented as a function of the water saturation S_w.

4.1 Direct P-waves phase velocity and attenuation measurements vs partial water saturation

The measured direct P-waves in Figure 6 are slower than sonic waves, since they lie in the [140 - 160] m/s range. The term "subsonic" P-waves is used, referring to the work of Michaels (2002) who commented on the validity of subsonic P-waves detection in very loose unconsolidated materials (Bachrach et al. 1998; Baker et al. 1999). In every sequence presented in Figure 6, V_P smoothly decreases as a function of an increasing S_w, both in imbibition and in drainage. It is important to note that the measured V_P are not constant from sequence to sequence : measured phase velocities V_P are slightly different for comparable S_w during I2, D2, I3 and D3. The decrease in V_P during imbibitions are also systematically steeper than the increase in V_P during drainages.

The inverse of the quality factor Q_P^{-1} or attenuation in Figure 6 varies vs S_w from sequence to sequence as well. The resulting quality factors are very low, ranging from 5 to 7.5, in agreement with typical expected values in unconsolidated media (Jeng et al. 1999; Molyneux & Schmitt 2000). Q_P^{-1} presents a rather different behavior between imbibition and drainage. During drainage, P-wave attenuation slightly decreases from $S_w \simeq 0.9$ to the residual water saturation $S_{w0} \simeq 0.3$. During imbibition, attenuation clearly reaches a maximum around $S_w = 0.6 - 0.7$ and varies monotonically on both sides of that maximum. Those cycles clearly reveal an hysteresis between imbibition and drainage, both during the cycle I2/D2 and the cycle I3/D3. The inverse quality factors are also very different during the four sequences, indicating certainly a quite rather different water fluid distribution as discussed below.

It is important to add that Q_P^{-1} continued to vary between the end of an imbibition and the start of a drainage, or vice-versa. As an example, Q_P^{-1} decreased by almost 20% while the water saturation kept constant ($S_w \simeq 0.85$) between the end of I3 and the beginning of D3. Due to technical difficulties, the sequences I2, D2, I3, D3 were not performed continuously in time, implying varying rest-time between imbibition an drainage. The largest rest-times for the water in the sand-filled tank, around fifteen hours, were between (I2-D2) and (D2-I3) whereas the shortest, between (I3-D3), was less than an hour.

We could not infer a clear and systematic behavior (increase or decrease) of the attenuation values during the rest-time. However, a qualitative explanation of these varying attenuation factors while the water is at rest might be advanced based on grain to grain contacts. The properties of fluid film between grains, which controls the visco-elastic behavior at the grain to grain contact, could be modified between each experiment. That idea is supported by the measured values of Q_P^{-1} for very low saturation values: since the drained bulk modulus K_D is defined as the bulk modulus of the slightly wet frame for unconsolidated media (Mavko et al. 1998), K_D should be measured in our experiment at the lowest saturation values, for the residual water saturation. Since the measured Q_P^{-1} for each sequence I2, D2, I3 and D3 are rather different for S_w in the $[0.3 - 0.4]$ range, that could mean that the K_D^* in equation (19) are different between sequences, leading to different values of Q_{K_D}. Various Q_{K_D} are then understood as an indicator of varying intergranular contacts between sequences in the context of the visco-elastic model discussed in section 2.5.

4.2 Discussion in light of the Biot theory

As suggested in section 2.2, the simplest way to interpret the measured velocities and quality factors seen in Figure 6 is to consider pure Biot's losses including an effective fluid model for ρ_f, η_f and K_f accounting for partial saturation. The decrease of phase velocities between the water and gas residual saturations observed experimentally is consistent with the computation presented in Figure 1 and is attributed to the increase of the total bulk density. It implies that wavelengths are much larger than the size of fluid heterogeneities and that pressure equilibration between the two phases is complete.

The computed velocities and inverse quality factors in Figure 1 cannot predict however the hysteresis observed between imbibition and drainage. That difference can be partly explained by effective pressure P_e variations (see part 2.3) since the pore fluid pressure might be significantly different between imbibition and drainage, whereas the computation in Figure 1 was performed for a constant P_e. Although P_e was not measured in the experiment, two possible effective pressure models can be proposed:

$$\begin{cases} P_e = (1-\phi)\rho_s\, g\, h \\ P_e(S_w) = (1-\phi)(\rho_s - S_w\, \rho_w)\, g\, h \end{cases} \tag{23}$$

where g is the gravity and $h = 0.17$ m is the sediment thickness above the measurement line. In the first model, the pore fluid pres-

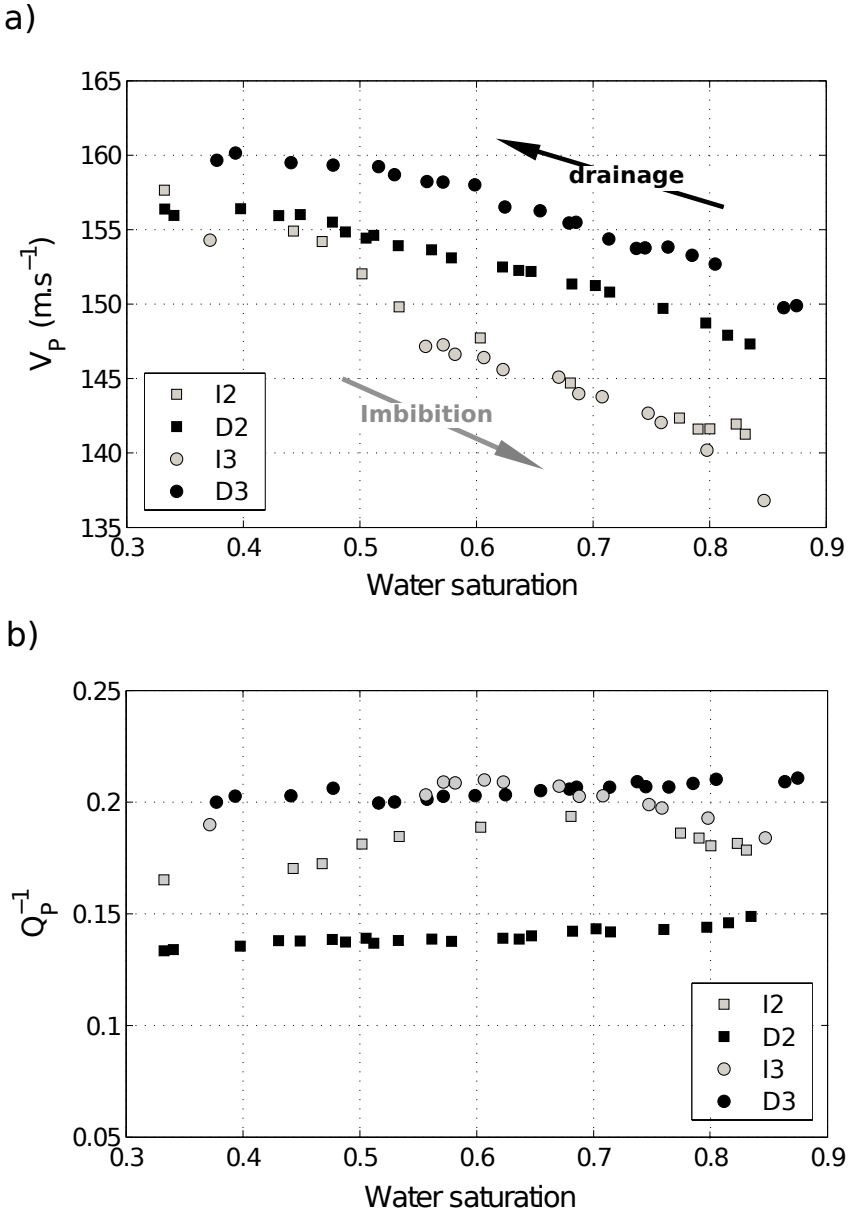

Figure 6. a) Measured P-waves phase velocity V_P and b) inverse quality factor Q_P^{-1} as a function of S_w, recorded during the second imbibition I2, the second drainage D2, the third imbibition I3 and the third drainage D3, for f = [1.6 - 1.8] kHz. The arrows in a) indicates that imbibition results in increasing S_w in time whereas drainage results in decreasing S_w. The experimental error-bars at each data point are shown in Figure 7.

sure is completely neglected and K_D, given by equation (17), corresponds to the bulk modulus of the dry frame. In the second model, the confining and pore pressures depend on the mass of the effective fluid contained in the sediment layer above the receivers. The effective bulk density of this upper layer is supposed homogeneous and equivalent to the one at the measurement depth. In the following, these two limit models of effective pressure are systematically considered in order to improve our analysis of the experimental measured phase velocity and quality factors.

The computation of the inverse quality factor in Figure 1b) vs S_w for a working frequency around 2 kHz is qualitatively in agreement with the measured attenuation during the two imbibitions: the theoretical and experimental values of Q_P^{-1} both have a maximum for a particular S_w. However, the theoretical Q_P^{-1} maximizes at $S_w = 0.8$ in Figure 1b) whereas it is around $S_w = 0.7$ (I2) and $S_w = 0.6$ (I3) in the experiments in Figure 6. The inverse quality factors obtained experimentally during drainages D2 and D3 are, in turn, not explained by Biot's model since they do not present any peak in the studied partial water saturation range. Lastly, the magnitude of the computed (< 0.035) and the measured (> 0.13) Q_P^{-1} strongly differ, the attenuation predicted by the Biot theory being clearly underestimated. In the following (section 4.4), this strong difference in amplitude will be compensated by the introduction of a visco-elastic contribution to the attenuation.

4.3 The role of effective permeability

We have shown in the previous section that the Biot theory coupled to an effective fluid model can explain qualitatively the gen-

eral trend of the measured V_P *vs* S_w and also the general trend of the measured Q_P^{-1} *vs* S_w during imbibition. The model cannot explain however the hysteresis between imbibition and drainage observed in Q_P^{-1} since the involved parameters ρ_f, η_f and K_f are by construction not sensitive to the saturation mode. At this stage, we propose to introduce the concept of relative permeabilities since those are usually considered as strongly dependent on the saturation mode.

No effective transport property was considered so far, assuming that the intrinsic permeability was completely available to the fluid mixture transport. It is known however that interactions between two fluids, water and gas in our case, are not negligible and can lead to a modification of their respective mobility, possibly leading to hysteresis phenomena between saturation modes. The relative permeabilities for water kr_w and gas kr_g, are defined as the part of intrinsic permeability respectively available for water and gas (Van Genuchten 1978; Pham et al. 2002):

$$kr_j = \sqrt{S_{je}}\left[1-(1-S_{je}^{1/m_j})^{m_j}\right]^2 \qquad \text{where } j=w,g. \tag{24}$$

The effective water and gas saturations S_{we} and S_{ge} depend on the water saturation S_w or gas saturation $S_g = 1-S_w$, and are defined by:

$$S_{je} = \frac{S_j - S_{j0}}{1-S_{j0}} \qquad \text{where } j=w,g. \tag{25}$$

The residual water and gas saturations S_{w0} and S_{g0} correspond to the flowing boundary for each phase: when $S_w < S_{w0}$, water cannot flow since the liquid phase is discontinuous and remain adsorbed by grains. When $S_w > 1-S_{g0}$, unconnected bubbles are jammed and trapped into the pore space. We suppose here that the residual water saturation $S_{w0} = 0.3$ is the lower saturation obtained during drainage and that the residual gas saturation $S_{g0} = 0.1$ is the complementary of the maximum water saturation obtained during imbibition. The values of the free parameters m_w and m_g, usually deduced from laboratory or field measurements, control the hysteresis phenomena through the shape of the kr_w and kr_g curves (Maqsoud et al. 2004). The relative permeabilities depend both on the saturation mode and the history of water content (number of previous cycles). The hysteresis can occur during an infinite number of cycles and is bordered by two limits that can be reached from the second cycle (Jensen & Falta 2005). As shown in the review by Jerauld & Salter (1990), the relative water permeability in unconsolidated porous media (sands or glass beads) is always lower during imbibition than during drainage, leading to m_w(imbibition)$\leq$ m_w(drainage) and to m_g(drainage)$\leq$ m_g(imbibition).

Taking into account the role of partial water saturation by the mean of relative permeabilities, it is then necessary to define the effective permeability involved in Biot's losses. The simplest model consists in considering that the mixture flow corresponds to the sum of gas and water flow. In this case, the effective permeability k_e is defined by:

$$k_e = k_0(kr_w + kr_g) \qquad \text{where} \qquad kr_w + kr_g \leq 1. \tag{26}$$

This expression implies that the effective permeability is lower than the intrinsic permeability except for $S_w = 0$ and $S_w = 1$. The monophasic permeability k_0 must therefore be substituted for the effective permeability k_e into Biot's frequency in equation (1) and in the m' parameter in equation (7). As shown in part 2.1, variations in fluid's properties and effective permeability also induce changes in the viscodynamic factor F. In order to account for those, the effective fluid model is applied by changing (η_f, ρ_f, k_0) in equation (8) by their effective values. Note that the geometrical parameter Λ^2 in equation (8) does not change in the effective model since it is an intrinsic parameter of the porous medium which does not depend on effective permeability. The viscodynamic operator F in (8) becomes:

$$F = \sqrt{1 + 4i\omega\frac{\gamma_0 k_e^2 \rho_f}{\xi \eta_f k_0 \phi}}. \tag{27}$$

4.4 Least-square inversion of Q_P^{-1} and V_P

We have advocated so far that the Biot theory coupled to the effective fluid model needs to be extended in order to properly interpret the measured velocities and inverse quality factors: we have introduced the concept of effective pressure variations $P_e(S_w)$, grain to grain losses (K_D^* or Q_{K_D}) and effective permeability $k_e(S_w)$. For this purpose:

- We will consider both models of effective pressure given in equation (23) which will, in turn, vary the bulk modulus K_D between models.
- We will introduce the visco-elastic intergranular losses into the Biot theory, as described in section 2.5, by using a constant-Q model involving two free parameters: the inverse quality factor $Q_{K_D}^{-1}$ and the reference angular frequency ω_0 of the visco-elastic model in equation (19). The choice of ω_0 is important regarding the phase velocity since it may introduce a strong phase velocity dispersion. The reference angular frequency shall respect the following criterion (Pham 2003):

$$\frac{1}{\pi Q_{K_D}}\left|\ln\frac{\omega}{\omega_0}\right| \ll 1 \tag{28}$$

which is met when ω_0 is close to the measurement angular frequency ω. We chose therefore to adjust $\omega_0 = 2\pi f_{max}$ to the maximum recorded frequency f_{max} (2 kHz in the experiment). $Q_{K_D^{-1}}$ remains the only visco-elastic free parameter that needs to be inverted from the experimental data.
- We have to estimate the two free parameters m_g and m_w involved in the effective permeability presented in section 4.3.

The three remaining unknown parameters in the final model ($Q_{K_D}^{-1}$, m_g and m_w) are inverted, in the least-squares sense, for the two effective pressure models. The joint inversion of V_P and Q_P^{-1} gives then two final poro-visco-elastic models for each cycle and saturation mode. Values of $Q_{K_D}^{-1}$ are explored in the $[0.05-0.25]$ range and values of m_g and m_w in the $[0.25-3.25]$ range.

The inverted parameters ($Q_{K_D}^{-1}$, m_g, m_w) for each imbibition and drainage are listed in Table 3 and the results of the least-square inversions are shown in Figure 7. The data V_P and Q_P^{-1} for each sequence are compared to the best inverted poro-visco-elastic model, for a constant effective pressure and for a varying pressure.

The P-waves phase velocities derived from the poro-visco-elastic model including the variable effective pressure are always lower than those derived with a constant effective pressure; that is a consequence of the decrease of K_D when the pore fluid pressure acts against the confinement pressure (see section 2.3), that decrease leading to lower V_P. We observe in Figure 7 that the measured phase velocities during both imbibitions are very well reproduced by the poro-visco-elastic model with a variable effective pressure. During both drainages, on the contrary, the measured velocities are consistent with the constant effective pressure model.

Cycle and saturation mode	Effective pressure model from equation (23)	$Q_{K_D}^{-1}$	m_w	m_g	Best least-square inversion model
I2	$P_e(S_w)$	0.12	1.05	2.05	*
	P_e	0.125	0.55	3.25	
D2	$P_e(S_w)$	0.09	1.125	1.025	
	P_e	0.09	1.1	1	*
I3	$P_e(S_w)$	0.14	0.525	2.35	*
	P_e	0.14	0.55	2.2	
D3	$P_e(S_w)$	0.14	1.525	3.25	
	P_e	0.14	1.175	1	*

Table 3. Table of parameters ($Q_{K_D}^{-1}$, m_g, m_w) obtained by least-square inversion of the measured V_P and Q_P^{-1} for each cycle and saturation mode, for two effective pressure model. The best poro-visco-elastic model for each sequence is shown with an asterisk *.

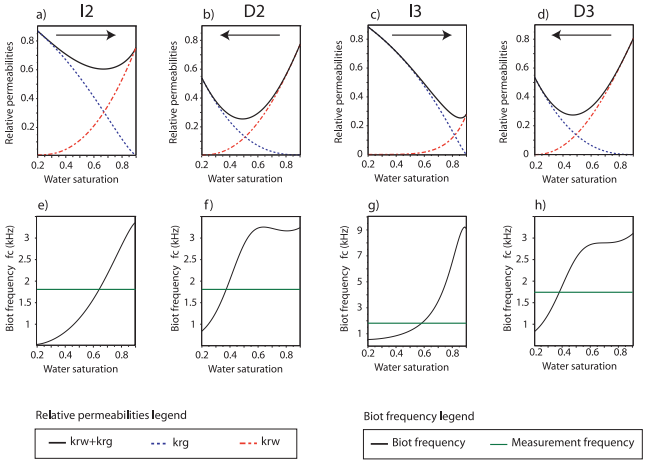

Figure 9. a) to d) Relative permeabilities k_{rw}, k_{rg} and normalized effective permeabilities $k_e/k_0 = k_{rw}+k_{rg}$ as a function of the water saturation S_w obtained during I2, D2, I3, and D3 respectively. The arrows indicates the direction of the evolution of S_w during the experiments. e) to h) Computed Biot's frequencies f_c using the effective permeabilities during I2, D2, I3, and D3 respectively. The horizontal solid line indicates the value of the experimental frequency, around 1.8 kHz.

Those two different models of V_P during imbibition and drainage are linked to the fluid circulation induced by our experimental procedures: during imbibition, a pressure charge is applied by uplifting a water tank above the sand-filled tank, whereas drainage is obtained by extracting water at a moderate flow rate with a pump. During pumping, an opposite pressure gradient is applied within the sand and the effect of pore pressure due to the weight of the fluid may be considerably reduced. In the following, accordingly, we consider that the adequate effective pressure models are: $P_e(S_w)$ for imbibitions and P_e for drainages (see equations 23). Concerning the comparison between data and models for the inverse quality factors in Figure 7, the effective pressure model seems to have less influence on the final inverse quality factors since both effective pressure model are close to data, both during imbibitions and drainages.

The quality of the inversion can be estimated in Figure 8 where the residuals of the least-square inversions are represented. For each sequence, as expected, the minimum in the residuals for $Q_{K_D}^{-1}$ is clearly marked: the best $Q_{K_D}^{-1}$ corresponds simply to a constant-Q increase from Biot's attenuation in order to attain the level of attenuation measured experimentally. Figure 8 then shows the (m_g, m_w) residuals maps at the previously found $Q_{K_D}^{-1}$. The data measured during D3 are remarkably inverted since the minimum of residuals are sharp in Figure 8d), the corresponding poro-visco-elastic model in red dashed line in Figure 7d) closely reproducing the velocities and attenuation data. The inversion for D2 presents also a well marked minimum in the (m_g, m_w) map but with bigger residuals compared to D3. The least-square inversions are somewhat less efficient for imbibitions in Figure 7a) and c), where the uncertainty on the best couple (m_g, m_w) are larger. Figure 7 shows nonetheless that even if residuals vary significantly between sequences, all experimental measurements both in V_P and Q_P^{-1} are satisfactorily reproduced by their corresponding final poro-visco-elastic model obtained by inversion.

4.5 Physical interpretation of the least-square inversion results

As predicted by Jerauld & Salter (1990), we have obtained m_w(imbibition) $\leq$ m_w(drainage) and m_g(drainage) $\leq$ m_g(imbibition) from the inversion for all the experiments (see Table 3). Using those values of (m_w, m_g) and the definitions of k_{rw} and k_{rg} given in equations (24) and (25), the relative permeabilities are shown as a function of the water saturation in Figure 9a)–d) for every sequence I2, D2, I3 and D3. Consistently, we observe in Figure 9 that k_{rg}(drainage) $\leq$ k_{rg}(imbibition) and k_{rw} (imbibition) $\leq$ k_{rw}(drainage). Those relative permeabilities values give indications about the fluid distribution within the pores. On the one hand, drainage may imply that the liquid phase remains continuous at the grain surfaces, draining first the biggest pores and making easier thereafter the entire fluid circulation. On the other hand, during imbibition the circulating water can more easily get trapped in gas pockets, thus leading to k_{rw} (imbibition) $\leq$ k_{rw}(drainage). We notice also in Figure 9a)–d) that the relative permeability values of each phase are very close during both drainages, indicating that the fluid circulation occurs with quite reproducible fluid distribution during drainages. On the contrary, during imbibition m_w(I2) $>$ m_w(I3) and consequently k_{rw}(I2) $>$ k_{rw}(I3), indicating that water circulation in the sand-filled tank was more difficult during I3 than during I2. As already mentioned, the third imbibition was performed after a fifteen hours rest-time whereas the second one was performed less than an hour after the first drainage. These different k_{rw} can be linked to the experimental procedure and to the fluid circulation within the pores: an imbibition performed just after the end of a drainage consists mainly in filling the largest pores just emptied by the drainage. Alternatively, when the rest-time is quite long after a drainage, the residual fluid rearranges within the entire pore space: the next imbibition consists then in filling fine as well as large pores, leading to a decreased relative water permeability compared to an imbibition performed quickly after a drainage.

The normalized effective permeabilities k_e/k_0 presented in Figures 9a)–d) are obtained by summing relative permeabilities as defined in equation (26). The effective permeabilities k_e are very similar during drainages and are rather different during imbibitions. The low relative water permeability during I3 leads in particular to a very low effective permeability around $k_e = 0.3k_0$ at the end of the imbibition in Figure 9c). At the beginning of the next drainage D3, however, we notice that the effective permeability is quite high, around $0.8k_0$, showing that the fluid was quickly rearranged in the pore space under the effect of pumping.

Biot's frequencies $f_c = (\phi\,\eta_f)/(2\pi\,\gamma_0\,\rho_f\,k_e)$ are represented in Figures 9e)–h) during every sequence as a function of water saturation. Whatever the saturation mode is, f_c globally increases

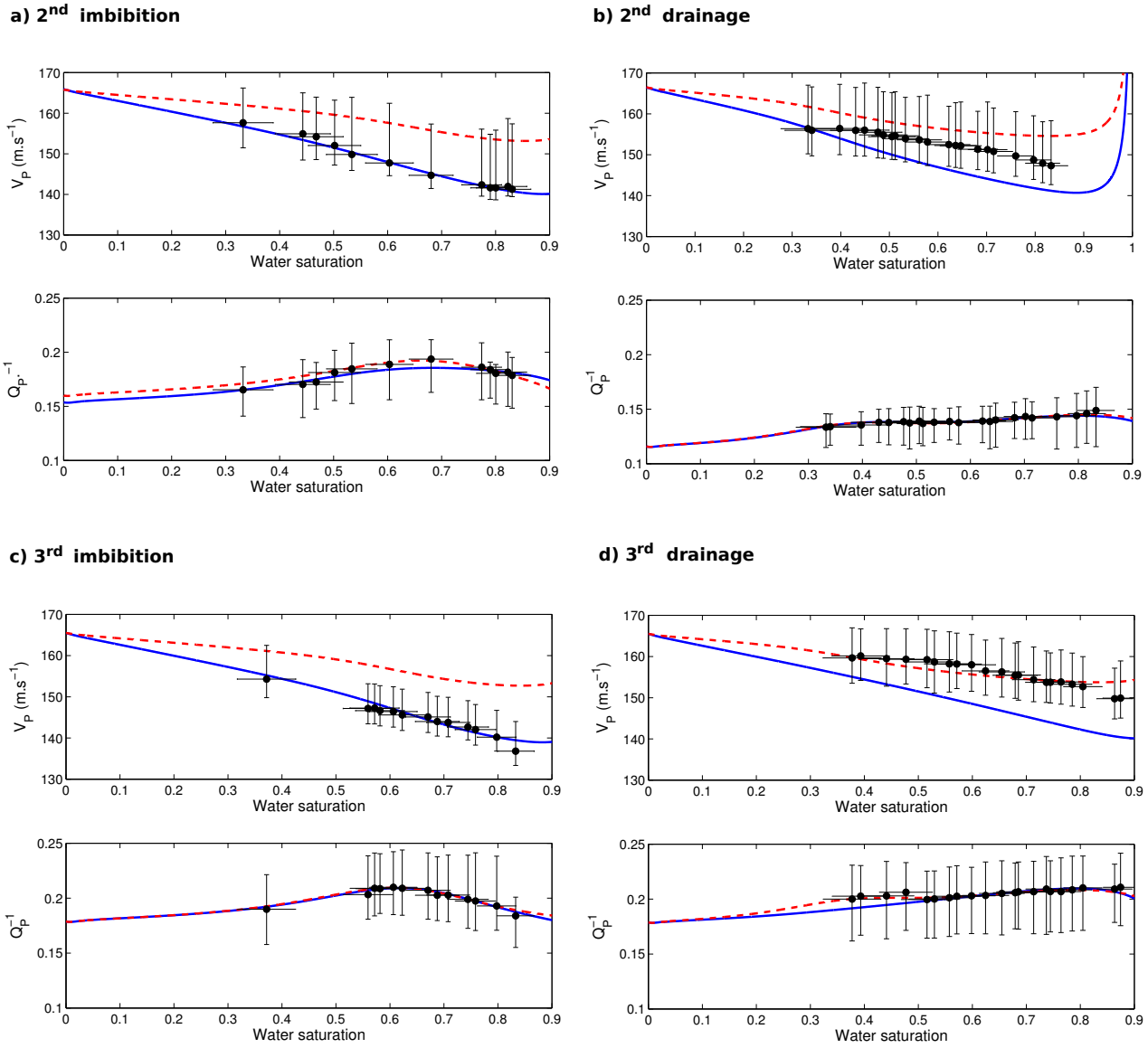

Figure 7. Comparison of the measured phase velocities and inverse quality factors with the final poro-visco-elastic model obtained by inversion for a) the second imbibition, b) the second drainage, c) the third imbibition and d) the third drainage. The experimental data are shown with black filled circles; errors bars derived from the experimental measurements are given for each measured data point. The red dashed lines are the best-fit models when the pore fluid pressure is completely neglected in the effective pore pressure. The blue solid line are the best-fit models corresponding to an effective pressure depending on the saturation as defined in equation (23).

vs water saturation and behaves like $\eta_f/(\rho_f\, k_e)$, the three variables depending on the saturation in Biot's frequency formula. It is then straightforward to see that the variations of the effective permeability $k_e(S_w)$, the only parameter varying between saturation modes, are going to modify the behavior of f_c vs S_w between drainages and imbibitions. During both drainages, f_c are relatively stable in the $S_w = [0.8 - 0.6]$ range, but strongly decrease in the $S_w = [0.6 - 0.2]$ range. During imbibitions, f_c increase progressively vs S_w. Moreover, the very low effective permeability measured during I3 results in a quite high Biot's frequency in Figure 9g) compared to the other experiments. Lastly, we notice that Biot's frequencies are equal to the measurement frequency (around 1.8 kHz) at $S_w \approx 0.4$ during both drainages and at $S_w \approx 0.6$ during both imbibitions.

In Biot's theory, the maximum in attenuation vs the frequency is reached when the measurement frequency coincides with f_c, $i.e.$ when the relative fluid/solid motion is the highest. In our experiments, when the water saturation varies, the petrophysical properties of the medium (ρ_f, η_f and k_e in particular) vary as well, possibly varying the mean attenuation level between S_w. We propose to discuss the evolution of Q_P^{-1} vs the water saturation and vs the frequency in Figure 10a)–d) for the poro-visco-elastic models of I3 and D3 obtained by inversion. Figures 10a) and c) show the inverse quality factors (same as in Figures 7b) and d)) for the constant effective pressure model during D3 and for the varying effective pressure model during I3, respectively. In Figure 10b), Q_P^{-1} for the poro-visco-elastic model during D3 is represented vs the frequency in the [1-3] kHz range, and is shown for different satura-

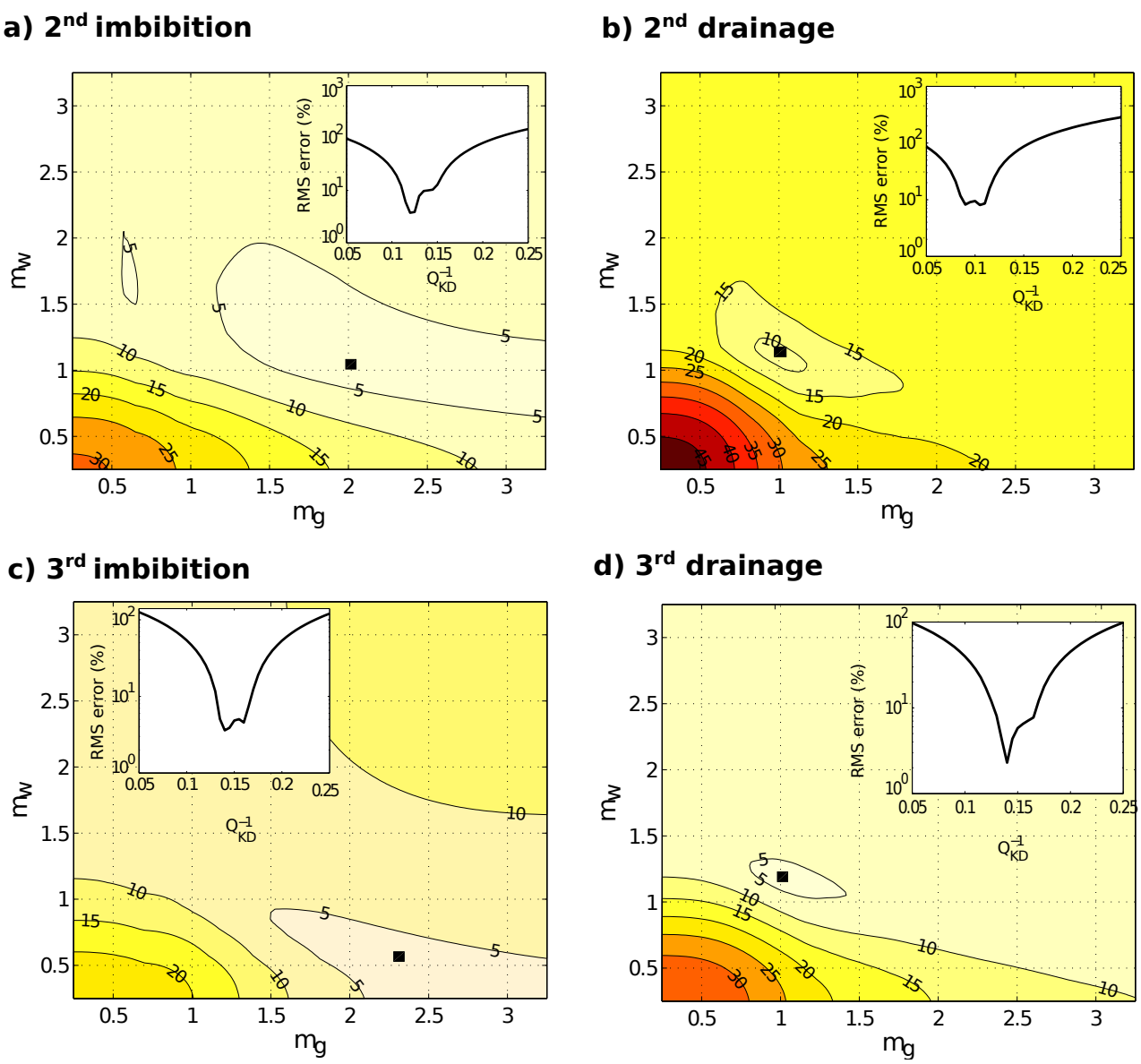

Figure 8. Least-square inversion residuals for $Q_{K_D}^{-1}$, and least-square inversion residuals maps (m_g, m_w) for the best $Q_{K_D}^{-1}$. The residuals are shown for the experiment I2, D2, I3, D3 in a), b), c) and d) respectively. The effective pressure is varying for I2 and I3 in a) and c), and is constant for D2 and D3 in b) and d) (see Table 3).

tions S_w: the advantage of this representation is that the petrophysical properties are constant for each S_w, and as expected from the Biot theory, the maximum in attenuation occurs when the measurement frequency coincides with f_c (S_w=0.6 during I3 and S_w=0.4 during D3 in Figures 7b) and d) respectively). It appears that the maximum in attenuation vs Sw in Figure 10a) is obtained in Figure 10b) around S_w=0.6 (point ④), where Biot's frequency f_c corresponds to the working frequency during I3.

For saturation values Sw below or above 0.6, Biot's frequency is remote from the measurement frequency (see Figure 9g)) and the attenuation is smaller than at $S_w = 0.6$, as it can be seen both in Figures 10a) and b). The same analysis in terms of Biot's frequency can be done during drainage D3 shown in Figures 10b) and d): an inflection point in attenuation is observed when f_c is around the working frequency, $i.e.$ around the point ② when $S_w = 0.4$ in Figures 10b) and d). However, for S_w above 0.4, although Biot's frequency shifts towards higher values compared to the measurement frequency (see Figure 9h)), the attenuation slightly continues to increase in Figure 10b) until $S_w = 0.7$, around ⑤. As mentioned above, the slight increase in attenuation may be attributed to mean different attenuation levels vs S_w, variations in attenuation due to variations in physical properties of the porous medium vs S_w. In particular, since the fluid mobility k_e/η_f is greater during D3 than during I3, the seismic dispersion could be responsible of the increase of the attenuation during D3, an increase not observed during I3 since the effective permeability was smaller (Batzle et al. 2006).

In short, we could expect intuitively that the maximum in attenuation vs S_w would be obtained at the saturation where the measurement frequency coincides with Biot's frequency. That was indeed observed during imbibition but not during drainage. As a matter of fact, the attenuation depends both on the vicinity of Biot's

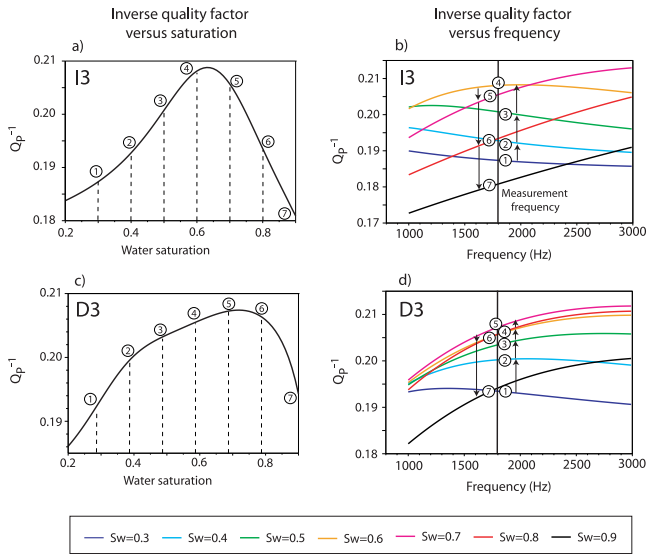

Figure 10. a) and c) Poro-visco-elastic models of the inverse quality factors deduced from the least-square inversion of the data measured during I3 and D3 respectively, as a function of the water saturation S_w. b) and d) Same poro-visco-elastic models of the inverse quality factors for I3 and D3 respectively as a function of the frequency. In b) and d) the various lines are computed for a constant S_w. The evolution of points from ① to ⑦ in b) and d) corresponds to the evolution of the same labelled points in a) and c) respectively. The vertical solid line indicates the value of the experimental frequency, around 1.8 kHz.

frequency and on the mean value of $Q_P^{-1}(\omega)$ depending on petrophysical properties. The measured attenuation during drainage does not therefore contradict Biot's theory.

5 CONCLUSIONS

The study of the effect of partial saturation on direct P-waves velocity and attenuation was conducted experimentally by monitoring a sand-filled tank during two imbibition/drainage cycles. The sand was highly permeable, homogeneous, with grain size diameters around 250 μm. The very low velocity of P-waves, around 150 m/s at our measurement frequency around 1.7 kHz, enabled to observe the wave-propagation along 10 wavelengths in our 1-m long apparatus. A Continuous Wavelet Transform applied on our seismic data recorded by buried accelerometers in the sand-filled tank, allowed to deduce the phase velocity V_P and the inverse quality factor Q_P^{-1} as a function of the partial saturation S_w for every experiment.

A systematic hysteresis between imbibition and drainage was observed in V_P and Q_P^{-1} vs S_w, as commonly measured in rocks (Knight & Nolen-Hoeksema 1990; Cadoret et al. 1995, 1998) but rarely in unconsolidated porous media (Domenico 1977; George et al. 2009) . In order to properly analyze our data, we have developped a generalized Biot's model including the following physical effects:

- Pure Biot's losses for an effective fluid (K_f, ρ_f, η_f) accounting for partial saturation;
- A varying effective pressure $P_e = P_c - P_f$ in the porous medium, where P_c is the confinement pressure and P_f the pore fluid pressure, following Walton's model;
- Grain to grain losses defined as a viscoelastic dissipation characterized by a constant $Q_{K_D}^{-1}$;
- An effective permeability $k_e = k_0(k_{rg} + k_{rw})$ depending on the saturation mode (imbibition or drainage) and characterized by two parameters m_w and m_g.

We have then performed a least-square inversion of the seismic data in order to determine $(Q_{K_D}^{-1},\ m_w,\ m_g)$ during the various experiments.

We have concluded from the inverted poro-visco-elastic models that V_P strongly depend on the mechanical properties of the effective fluid and on the effective pressure: during imbibition, the fluid injection increases P_f and V_P decrease as a function of S_w. During drainage, V_P still decrease vs S_w but less rapidly since P_f is negligible. We have also concluded from the inversions that the major part of the high inverse quality factors Q_P^{-1} measured is attributed to the constant-Q visco-elastic grain to grain energy dissipation. The fluctuations of Q_P^{-1} vs S_w, on the top of this constant-Q model, are then satisfactorily explained at the first order by pure Biot's losses taking into account the effective fluid properties. Lastly, the variations of effective permeability from experiment to experiment explain the final form of Q_P^{-1} vs S_w; the effective permeability associated to different fluid distributions in the porous medium is responsible of the observed hysteresis between imbibition and drainage. We have understood that the experimental procedures used to proceed to an imbibition or a drainage, in particular the rest-time between an imbibition and a drainage, can be responsible of significant variations both in the lubrication of the grain to grain contact and in the fluid distribution in the pore space: the viscoelastic component of the attenuation ($Q_{K_D}^{-1}$) and the effective permeability of the porous media can quickly change from experiment to experiment as revealed by the least-square inversions.

We have also analyzed the measured Q_P^{-1} vs S_w in terms of variations of the Biot's frequency f_c during the experiments. As we are proceeding to an imbibition or a drainage, the petrophysical physical properties of the medium change as a function of time, since during the experiment ρ_f, η_f and k_e are changing. The Biot's frequency values therefore fluctuate during an experiment. We have concluded that in our experiments, the maximum in attenuation vs S_w is not systematically observed when the measurement frequency coincides with the Biot's frequency.

Our experiment shows that the fluid distribution in the porous medium has a strong influence on inverse quality factors. It confirms that seismic prospection can provide essential informations on the fluid content and distribution in geological reservoirs. In the frequency range we have explored, the contribution of grain to grain losses dominates since we chose to work on unconsolidated media. Nevertheless, the Biot's theory remains an efficient approach in order to understand the fluctuations of both velocities and attenuation in partially saturated sands since wavelengthes are larger than the fluid heterogeneities. The understanding of the observed phenomena could be improved by further experiments: the measurement of the effective pressure could be, for example, a key parameter to constrain the poro-visco-elastic models. Broadband seismic signals could also be a significant progress since it would provide a complete dynamical study of phase velocities and attenuation in unconsolidated media. Furthermore, some theoretical models obtained by extending Biot's equations could account for capillary pressure and interactions between air and water at the pore scale (Santos et al. 1990; Tuncay & Corapcioglu 1997; Lo et al. 2005).

6 ACKNOWLEDGEMENTS

This study has benefited to the ANR program of the French government, especially via the TRANSEK project. The authors thanks S. Garambois (ISTerre, France), Y. Gueguen (ENS Paris, France), K. Holliger (UNIL, Switzerland), M. Tygel (UniCAMP, Brasil) for their constructive interactions.

REFERENCES

Aki, K. & Richards, P. G., 2002. *Quantitative Seismology, 2nd Ed. K. Aki and P.G Richards, editors.*, University Science Books.

Ayres, A. & Theilen, F., 2001. Preliminary laboratory investigations into the attenuation of compressional and shear waves on near-surface marine sediments, *Geophysical Prospecting*, **49**, 120–127.

Bachrach, R. & Nur, A., 1998. High-resolution shallow-seismic experiments in sand, part i: Water table, fluid flow, and saturation, *Geophysics*, **63**, 1225.

Bachrach, R., Dvorkin, J., & Nur, A., 1998. High-resolution shallow-seismic experiments in sand, part ii: Velocities in shallow unconsolidated sand, *Geophysics*, **63**, 1234.

Badiey, M., Cheng, A., & Mu, Y., 1998. From geology to geoacoustics–evaluation of biot-stoll sound speed and attenuation for shallow water acoustics, *Acoustical Society of America Journal*, **103**, 309–320.

Baker, G. S., Schmeissner, C., Steeples, D. W., & Plumb, R. G., 1999. Seismic reflections from depths of less than two meters, *Geophysical Research Letters*, **26**, 279–282.

Bardet, J. P. & Sayed, H., 1993. Velocity and attenuation of compressional waves in nearly saturated soils, *Soil Dynamics and Earthquake Engineering*, **12**, 391–401.

Baron, L. & Holliger, K., 2011. Constraints on the Permeability Structure of Alluvial Aquifers From the Poro-Elastic Inversion of Multifrequency P-Wave Sonic Velocity Logs, *IEEE Transactions on Geoscience and Remote Sensing*, **49**, 1937–1948.

Barrière, J., 2011. *Attenuation et dispersion des ondes P en milieu poreux partiellement saturé : Approche exprimentale*, Ph.D. thesis, Université de Pau et des Pays de l'Adour.

Batzle, M. L., Han, D.-H., & Hofmann, R., 2006. Fluid mobility and frequency-dependent seismic velocity : Direct measurements, *Geophysics*, **71**, 1.

Berge, P. A. & Bonner, B. P., 2002. Seismic velocities contain information about depth, lithology, fluid content and microstructure, *pp. UCRL-JC-144792, Symposium on the Application of Geophysics to Engineering and Environmental Problems*.

Berryman, J. G., 1981. Elastic wave propagation in fluid-saturated porous media, *Acoustical Society of America Journal*, **69**, 416–424.

Berryman, J. G., Thigpen, L., & Chin, R. C. Y., 1988. Bulk elastic wave propagation in partially saturated porous solids, *Acoustical Society of America Journal*, **84**, 360–373.

Biot, M. A., 1956a. Theory of propagation of elastic waves in a fluid-saturated porous solid. i. low-frequency range, *Acoustical Society of America Journal*, **28**, 168.

Biot, M. A., 1956b. Theory of propagation of elastic waves in a fluid-saturated porous solid. ii. higher frequency range, *Acoustical Society of America Journal*, **28**, 179.

Biot, M. A., 1962. Mechanics of deformation and acoustic propagation in porous media, *Journal of Applied Physics*, **33**, 1482–1498.

Biot, M. A. & Willis, D. G., 1957. The influence of the theory of consolidation, *J. Appl. Mech.*, **24**, 594–601.

Bordes, C., Jouniaux, L., Dietrich, M., Pozzi, J.-P., & Garambois, S., 2006. First laboratory measurements of seismo-magnetic conversions in fluid-filled fontainebleau sand, *Geophys. Res. Lett.*, **33**, LO1302.

Bordes, C., Jouniaux, L., Garambois, S., Dietrich, M., Pozzi, J.-P., & Gaffet, S., 2008. Evidence of the theoretically predicted seismo-magnetic conversion, *Geophysical Journal International*, **174**, 489–504.

Bourbié, T., Coussy, O., & Zinszner, B., 1987. *Acoustics of porous media*, ditions Technip.

Buchanan, J. L., 2006. A comparison of broadband models for sand sediments, *Acoustical Society of America Journal*, **120**, 3584.

Cadoret, T., Marion, D., & Zinszner, B., 1995. Influence of frequency and fluid distribution on elastic wave velocities in partially saturated limestones, *J. Geophys. Res.*, **100**(B6), 9789–9803.

Cadoret, T., Mavko, G., & Zinszner, B., 1998. Fluid distribution effect on sonic attenuation in partially saturated limestones, *Geophysics*, **63**, 154.

Carcione, J. M., 2001. *Wave fields in real media : Wave propagation in anelastic, anisotropic and porous media*, Pergamon, Elsevier Science Ltd.

Chotiros, N. P. & Isakson, M. J., 2004. A broadband model of sandy ocean sediments: Biot-stoll with contact squirt flow and shear drag, *Acoustical Society of America Journal*, **116**, 2011–2022.

Daley, T. M., Myer, L. R., Peterson, J. E., Majer, E. L., & Hoversten, G. M., 2008. Time-lapse crosswell seismic and VSP monitoring of injected CO_2 in a brine aquifer, *Environmental Geology*, **54**, 1657–1665.

Domenico, S. N., 1977. Elastic properties of unconsolidated porous sand reservoirs, *Geophysics*, **42**, 1339.

Duffaut, K., Landro, M., & Sollie, R., 2010. Using mindlin theory to model friction-dependent shear modulus in granular media, *Geophysics*, **75**, 143–152.

Dvorkin, J., 1993. Dynamic poroelasticity: A unified model with the squirt and the biot mechanisms, *Geophysics*, **58**, 524.

Futterman, W. I., 1962. Dispersive body waves, *jgr*, **67**, 5279–5291.

Gassmann, F., 1951. Uber die elastizitt porser medien, *Vierteljahrsschrift der Naturforschenden Gesellschaft in Zurich*, **96**, 1–23.

George, L. A., Dewoolkarb, M. M., & Znidarcicc, D., 2009. Simultaneous laboratory measurement of acoustic and hydraulic properties of unsaturated soils, *Vadoze Zone Journal*, **8**, 633–648.

Gist, G. A., 1994. Interpreting laboratory velocity measurements in partially gas-saturated rocks, *Geophysics*, **59**(7), 1100–1109.

Gregory, A. R., 1976. Fluid saturation effects on dynamic elastic properties of sedimentary rocks, *Geophysics*, **41**, 895.

Gurevich, B., Makarynska, D., de Paula, O. B., & Pervukhina, M., 2010. A simple model for squirt-flow dispersion and attenuation in fluid-saturated granular rocks, *Geophysics*, **75**, 109.

Haase, A. B. & Stewart, R. R., 2010. Near-field seismic effects in a homogeneous medium and their removal in vertical seismic profile attenuation estimates, *Geophysical Prospecting*, **58**, 1023–1032.

Hefner, B. T. & Williams, K. L., 2006. Sound speed and attenuation measurements in unconsolidated glass-bead sediments saturated with viscous pore fluids, *Acoustical Society of America Journal*, **120**, 2538.

Jeng, Y., Tsai, J. Y., & Chen, S. H., 1999. An improved method of determining near-surface q, *Geophysics*, **64**(5), 1608–1617.

Jensen, K. H. & Falta, R. W., 2005. *Fundamentals. In A.S. Mayer and S.M Hassanizadeh, editors, Soil and Groundwater Contamination : Nonaqueous Phase Liquids*, American Geophysical Union, 2000 Florida Avenue, N.W., Washington D.C 20009, US.

Jerauld, G. R. & Salter, S. J., 1990. The effect of pore structure on hysteresis in relative permeability and capillary pressure: Pore-level modelling, *Transport in porous media*, **5**, 103–151.

Johnson, D. L., 2001. Theory of frequency dependent acoustics in patchy-saturated porous media, *Acoustical Society of America Journal*, **110**, 682.

Johnson, D. L., Koplik, J., & Dashen, R., 1987. Theory of dynamic permeability in fluid saturated porous media, *J. Fluid. Mech.*, **176**, 379–402.

Johnston, D. H., Toksöz, M. N., & Timur, A., 1979. Attenuation of seismic waves in dry and saturated rocks: Ii. mechanisms, *Geophysics*, **44**, 691.

Kazemeini, S. H., Juhlin, C., Zinck-Jørgensen, K., & Norden, B., 2009. Application of the continuous wavelet transform on seismic data for mapping of channel deposits and gas detection at the co2sink site, ketzin, germany, *Geophysical Prospecting*, **57**, 111–123.

Keller, J. D., 1989. Acoustic wave propagation in composite fluid-saturated media, *Geophysics*, **54**, 1554.

Kimura, M., 2006. Frame bulk modulus of porous granular marine sediments, *Acoustical Society of America Journal*, **120**, 699.

King, M. S., Marsden, J. R., & Dennis, J. W., 2000. Biot dispersion for p- and s-waves velocities in partially and fully saturated sandstones, *Geo-*

physical Prospecting, **48**, 1075–1089.

Kjartansson, E., 1979. Constant q-wave propagation and attenuation, *J. Geophys. Res.*, **84**, 4737–4748.

Knight, R. & Nolen-Hoeksema, R., 1990. A laboratory study of the dependence of elastic wave velocities on pore scale fluid distribution, *Geophys. Res. Lett.*, (17), 1529–1532.

Komatitsch, D. & Vilotte, J. P., 1998. The spectral-element method: an efficient tool to simulate the seismic response of 2D and 3D geological structures, *Bull. Seismol. Soc. Am.*, **88**(2), 368–392.

Lang, W. C. & Forinash, K., 1998. Time-frequency analysis with the continuous wavelet transform, *American Journal of Physics*, **66**, 794–797.

Lebedev, M., Toms-Stewart, J., Clennell, B., Pervukhina, M., Shulakova, V., Paterson, L., M., M. T., Gurevich, B., & Wenzlau, F., 2009. Direct laboratory observation of patchy saturation and its effects on ultrasonic velocities, *The Leading Edge*, **28**(1), 24–27.

Lo, W., Sposito, G., & Majer, E., 2005. Wave propagation through elastic porous media containing two immiscible fluids, *Water Resources Research*, **41**, 2025.

Mangriotis, M., Rector, J. W., & Herkenhoff, E. F., 2011. Effects of the near-field on shallow seismic studies, *Geophysics*, **76**, 9.

Maqsoud, A., Bussire, B., Mbonimpa, M., & Aubertin, M., 2004. Hysteris effects on the water retention curve : A comparison between laboratory results and predictive models, *57th Canadian Geotechnical Conference, 5th Joint CGS/IAH-CNC Conference*, **Session 3A**, 8–15.

Mavko, G. & Nolen-Hoeksema, R., 1994. Estimating seismic velocities at ultrasonic frequecies in partially saturated rocks., *Geophysics*, **59**(2), 252–258.

Mavko, G. & Nur, A., 1979. Wave attenuation in partially saturated rocks, *Geophysics*, **44**(2), 161–178.

Mavko, G., Mukerji, T., & Dvorkin, J., 1998. *The rock physics handbook: Tools for seismic analysis in porous media*, Cambridge University Press, The Pitt Building, Trumpington Street, Cambridge CB2 IRP, United Kingdom.

Michaels, P., 2002. Identification of subsonic p-waves, *Geophysics*, **67**, 909.

Mindlin, R. D., 1949. Compliance of elastic bodies in contact, *Journal of Applied Mechanics*, **16**, 259–268.

Molyneux, J. B. & Schmitt, D. R., 2000. Compressional-wave velocities in attenuating media: A laboratory physical model study, *Geophysics*, **65**, 1162.

Monsen, K. & Johnstad, S. E., 2005. Improved understanding of velocity-saturation relationships using 4d computer-tomography acoustic measurements, *Geophysical Prospecting*, **53**, 173–181.

Muller, T. M., Gurevich, B., & Lebedev, M., 2010. Seismic wave attenuation and dispersion resulting from wave-induced flow in porous rocks : A review, *Geophysics*, **75**(26), A260000+.

Murphy, W. F., 1984. Acoustic measures of partial gas saturation in tight sandstones, *Journal of Geophysical Research*, **89**, 11549–11560.

Murphy, III, W. F., 1982. Effects of partial water saturation on attenuation in massilon sandstone and vycor porous glass, *Acoustical Society of America Journal*, **71**, 1458–1468.

Parra, J., Hackert, C., Richardson, E., & Clayton, N., 2009. Porosity and permeability images based on crosswell seismic measurements integrated with fmi logs at the port mayaca aquifer, *The Leading Edge*, **28**, 1212–1219.

Pham, N. H., 2003. *Wavefields in porous media: lithology, pressure and saturation effects*, Thesis presented for the degree of Doctor of Engineering of the Norwegian University of science and Technology, Department of Petroleum Engineering and Applied Geophysics.

Pham, N. H., Carcione, J. M., Helle, H. B., & Ursin, B., 2002. Wave velocities and attenuation of shaley sandstones as a function of pore pressure and partial saturation, *Geophysical Prospecting*, **50**, 615–627.

Prasad, M., 1992. Attenuation mechanisms in sands: Laboratory versus theoretical (biot) data, *Geophysics*, **57**, 710.

Prasad, M., 2002. Acoustic measurements in unconsolidated sands at low effective pressure and overpressure detection, *Geophysics*, **67**, 405.

Pride, S. R., 2005. *Relationships between seismic and hydrological properties. In Y. Rubin and S.S. Hubbard, editors, Hydrogeophysics*, Springer, Water sciences and technology library.

Pride, S. R., Berryman, J. G., & Harris, J. M., 2004. Seismic attenuation due to wave-induced flow, *Journal of Geophysical Research (Solid Earth)*, **109**, 1201.

Reine, C., van der Baan, M., & Clark, R., 2009. The robustness of seismic attenuation measurements using fixed- and variable-window time-frequency transforms, *Geophysics*, **74**, 123.

Rubino, J. G. & Holliger, K., 2012. Seismic attenuation and velocity dispersion in heterogeneous partially saturated porous rocks, *Geophysical Journal International*, **188**, 1088–1102.

Santos, J. E., Douglas, Jr., J., Corberó, J., & Lovera, O. M., 1990. A model for wave propagation in a porous medium saturated by a two-phase fluid, *Acoustical Society of America Journal*, **87**, 1439–1448.

Sénéchal, P., Garambois, S., & Bordes, C., 2010. Feasibility of acoustic imaging for in-situ characterization of subsurface soil injected with fresh mortar, *Journal of Applied Geophysics*, **72**, 184–193.

Shepard, D., 1968. A two-dimensional interpolation function for irregularly-spaced data, *Proceddings of the 1968 ACM National Conference*, pp. 517–524.

Skempton, A. W., 1954. The pore-pressure coefficients a and b, *Geotechnique*, **4**, 143–147.

Stoll, R. D., 1977. Acoustic waves in ocean sediments, *Geophysics*, **42**, 715.

Stoll, R. D. & Bryan, G. M., 1970. Wave attenuation in saturated sediments, *Acoustical Society of America Journal*, **47**, 1440.

Teja, A. S. & Rice, P., 1981. Generalized corresponding states method for viscosities of liquid mixtures, *Industrial Engineering Chemistry Fundamentals*, **20**, 77–81.

Toms, J., Müller, T. M., Ciz, R., & Gurevich, B., 2006. Comparative review of theoretical models for elastic wave attenuation and dispersion in partially saturated rocks, *Soil Dynamics and Earthquake Engineering*, **26**, 548–565.

Tromp, J., Komatitsch, D., & Liu, Q., 2008. Spectral-element and adjoint methods in seismology, *Communications in Computational Physics*, **3**(1), 1–32.

Tuncay, K. & Corapcioglu, M. Y., 1997. Wave propagation in poroelastic media saturated by two fluids, *Journal of Applied Mechanics*, **64**, 313.

Turgut, A., 1991. *An investigation of causality for Biot models by using Kramers-Kronig relations. In J.M. Hovem, M.D. Richardson, and R.D. Stoll, editors, Shear Waves in Marine Sediments*, Kluwer Academic Publishers.

Van Genuchten, R., 1978. *Calculating the unsaturated hydraulic conductivity with a closed form analytical model*, Report 78-WR-08, Princeton University, NJ.

Vasco, D. W., Datta-Gupta, A., Behrens, R., Condon, P., & Rickett, J., 2004. Seismic imaging of reservoir flow properties: Time-lapse amplitude changes, *Geophysics*, **69**, 1425.

Walsh, J. B., 1966. Seismic wave attenuation in rock due to friction, *Journal of Geophysical Research*, **71**, 2591.

Walsh, J. B., 1995. Seismic attenuation in partially saturated rock, *Journal of Geophysical Research*, **1001**, 15407–15424.

Walton, K., 1987. The effective elastic moduli of a random packing of spheres, *Journal of Mechanics Physics of Solids*, **35**, 213–226.

White, J. E., 1975. Computed seismic speeds and attenuation in rocks with partial gas saturation, *Geophysics*, **40**, 224.

Winkler, K. W. & Plona, T. J., 1982. Technique for measuring ultrasonic velocity and attenuation spectra in rocks under pressure, *Journal of Geophysical Research*, **87**, 10776–10780.

Wood, A. W., 1955. *A Textbook of Sound*, The MacMillan Co.

Wuenschel, P. C., 1965. Dispersive body waves : An experimental study, *Geophysics*, **30**, 539.